Chemical vapor deposited graphene and transition metal dichalcogenide nanoflake heterostructures

Petri Mustonen

School of Electrical Engineering

Thesis submitted for examination for the degree of Master of Science in Technology.

Espoo 31.7.2017

Thesis supervisor:

Prof. Harri Lipsanen

Thesis advisor:

M.Sc. Changfeng Li

Aalto University
School of Electrical
Engineering

AALTO UNIVERSITY
SCHOOL OF ELECTRICAL ENGINEERING

ABSTRACT OF THE
MASTER'S THESIS

Author: Petri Mustonen

Title: Chemical vapor deposited graphene and transition metal dichalcogenide nanoflake heterostructures

Date: 31.7.2017 Language: English Number of pages: 5+54

Department of Electronics and Nanoengineering

Professorship: Advanced Materials and Photonics Code: ELEC3035

Supervisor: Prof. Harri Lipsanen

Advisor: M.Sc. Changfeng Li

Transition Metal Dichalcogenides (TMDs) offer new and complementary properties to those of graphene. It is of much interest to manufacture heterostructures of these materials to fully exploit their properties. Traditionally these heterostructures are manufactured by mechanically exfoliating small flakes from large bulk crystal and then manually aligning the flakes. This is a slow and cumbersome process.
In this thesis, it is analyzed whether graphene can be directly grown on top of chemically exfoliated TMD flakes via Chemical Vapor Deposition (CVD) on copper substrates in order to significantly increase throughput. At first the thermal stability of the following TMDs were tested: Molybdenum Disulfide (MoS_2), Tungsten Disulfide (WS_2) and hexagonal Boron Nitride (hBN). It was concluded that only hBN has the thermal stability to be used in a standard methane based CVD graphene process.
Initial experiments with chemically exfoliated hBN flakes gave inconclusive results due to the confocal Raman spectrography not offering resolutions high enough to map the surface of the flakes after CVD growth. However, the experiments lead to the conclusion that CVD graphene does not grow under the flakes via intercalation or precipitation. Lorentzian-peak center-position filter was developed to distinguish small hBN nanoflakes from the midst of defective graphene. Mechanically exfoliated hBN flakes were used to overcome the resolution limitation of confocal Raman spectroscopy. The results indicate that CVD graphene can grow on the flakes only if there are defects on the hBN flake surface. However, graphene growth is inconsistent and does not fully cover the flake.

Keywords: Chemical vapor deposition, transition metal dichalcogenides, graphene, heterostructures, Raman spectroscopy

AALTO-YLIOPISTO
SÄHKÖTEKNIIKAN KORKEAKOULU

DIPLOMITYÖN
TIIVISTELMÄ

Tekijä: Petri Mustonen

Työn nimi: Kaasufaasidepositioidun grafeenin ja siirtymämetallidikalkogenidi nanohiutaleiden heterorakenteet

Päivämäärä: 31.7.2017 Kieli: Englanti Sivumäärä: 5+54

Elektroniikan ja nanotekniikan laitos

Professuuri: Uudet materiaalit ja fotoniikka Koodi: ELEC3035

Työn valvoja: Prof. Harri Lipsanen

Työn ohjaaja: DI. Changfeng Li

Siirtymämetallidikalkogenidit (TMDt) tarjoavat grafeenia täydentäviä ominaisuuksia ja näiden materiaalien välisillä heterorakenteilla voidaan yhdistää materiaalien parhaita puolia. Tavallisesti heterorakenteiden valmistaminen tapahtuu mekaanisesti eksfolioimalla (kuorimalla) ohuita hiutaleita suuremmasta kiderakenteesta ja manuaalisesti asettamalla hiutaleet paikoilleen. Tämä on hidas ja vaivalloinen prosessi.

Tässä työssä tutkitaan grafeenin kasvattamista kaasufaasidepositiolla suoraan kemiallisesti eksfolioitujen TMD-hiutaleiden päälle, mikä onnistuessaan helpottaisi ja nopeuttaisi heterorakenteiden valmistamista.

Ensimmäisessä vaiheessa tutkittiin TMD-materiaalien lämpötilakestävyyttä. Tutkitut materiaalit olivat molybdeenidisulfidi (MoS_2), wolframdisulfidi (WS_2) ja heksagonaalinen boorinitridi (hBN). Osoittautui, että vain hBN kestää korkean lämpötilan, jonka grafeenin kasvatus metaanipohjaisella kaasufaasidepositiolla vaatii.

Grafeenin kasvamista kemiallisesti eksfolioitujen nanokokoisten hBN-hiutaleiden pinnalle ei saatu analysoitua, koska työssä käytetyn konfokaalisen Raman-spektroskopian resoluutio ei ollut riittävä hiutaleiden pinnan kuvantamiseen kasvatusprosessin jälkeen. Näitä hBN-hiutaleita pystyttiin kuitenkin hyödyntämään, kun tutkittiin grafeenin kasvua niiden alle. Tulosten perusteella voidaan sanoa, että grafeeni ei kasva nanokokoisten hBN-hiutaleiden alle.

Työn ohessa kehitettiin Lorentz-sovitukseen perustuva suodatin, jolla saadaan erotettua toisistaan hBN nanohiutaleet huonolaatuisesta grafeenista.

Grafeenin kasvatuksen jatkoanalyysissä käytettiin mekaanisesti eksfolioituja hBN-hiutaleita aikaisemmin mainitun konfokaalisen Raman-spektroskopian resoluutiorajoitteen takia. Jatkoanalyysissä havaittiin, että grafeeni voi kasvaa TMD-hiutaleiden päälle vain, jos niissä on rakenteellisia virheitä.

Avainsanat: Kaasufaasidepositio, siirtymämetallidikalkogenidit, grafeeni, heterorakenteet, Raman-spektroskopia

Preface

This thesis was written in the Department of Electronics and Nanoengineering to complete the requirements of Master's Programme in Nano and Radio Sciences (NANORAD) in Aalto University School of Electrical Engineering.

I give my sincerest gratitude to Professor Harri Lipsanen for granting me the opportunity to work in the graphene group and for all his advice during my thesis. I am also grateful for all the conversations and help I received regarding my thesis from Joonas Holmi, Maria Kim and my advisor Changfeng Li. Furthermore, I would like to extend my gratitude to the entire graphene group all of whom have helped me to complete my thesis. I also give my thanks to Iurii Kim and Wonjae Kim for their help on my thesis and on my research and Akseli Kohtamäki for his help on practical matters here in Micronova.

I am wholeheartedly grateful for the support and patience of my fiancée Ella Piiroinen, my mother Anneli Mustonen, my sister Annemari Mustonen and especially my father Mika Mustonen for his suggestions and ideas concerning the textual presentation and appearance of my thesis.

Espoo, 31.7.2017

Petri M. Mustonen

Contents

Symbols and abbreviations

Abbreviations

2-D	Two-dimensional
2D-band	The 2nd major Raman band of graphene at ∼2600–2750 cm^{-1}
BSE	Backscattered electron
CCD	Charge-Coupled Device
CMOS	Complementary Metal-Oxide–Semiconductor
Cu	Copper
CVD	Chemical Vapor Deposition
D-band	The Raman disorder band of graphene at ∼1300–1400 cm^{-1}
DFT	Density Functional Theory
DI-water	Deionized water
EDX	Energy-dispersive X-ray spectroscopy
EELS	Electron Energy Loss Spectroscopy
EHF	Extremely High Frequency
EM	Electromagnetic
EMCCD	Electron Multiplying Charge-Coupled Device
E-T	Everhart-Thornley
FET	Field Effect Transistor
G-band	The 1st major Raman band of graphene at ∼1300–1400 cm^{-1}
hBN	Hexagonal Boron Nitride
HEMT	High Electron Mobility Transistor
HOPG	Highly Oriented Pyrolytic Graphite
InP	Indium Phosphide
MBE	Molecular Beam Epitaxy
MOCVD	Metal-Organic Chemical Vapor Deposition
MoS_2	Molybdenum Disulfide
MoX_2	Molecule consisting of molybdenum and a dichalcogenide
MX_2	Molecule consisting of a transition metal and a dichalcogenide
NA	Numerical aperture of a lens
NM	Nanomembrane
NW	Nanowire
PDMS	Polydimethylsiloxane
PECVD	Plasma Enhanced Chemical Vapor Deposition
PMMA	Polymethyl Methacrylate
RIE	Reactive Ion Etching
SEM	Scanning Electron Microscope
Si	Silicon
SiC	Silicon Carbide
SiO_2	Silicon dioxide
SiO_2/Si	Silicon substrate with an insulating oxide layer on top
STM	Scanning Tunneling Microscopy
TEM	Transmission Electron Microscopy
TMD	Transition Metal Dichalcogenide
UHV	Ultra-High Vacuum
WS_2	Tungsten Disulfide
WX_2	Molecule consisting of tungsten and a dichalcogenide

1 Introduction

Graphene is a two-dimensional (2-D) allotrope of carbon, the first 2-D material discovered, which started a new era of nanomaterials. It was quickly observed that it has properties that far exceed that of any bulk (3-D) material. For instance, it can conduct heat and electricity extremely well, while still being flexible, stretchable, transparent and extremely strong in comparison to its minute thickness.

Numerous other 2-D materials that have vastly different properties than their bulk version have been discovered after graphene, including a group of materials called Transition Metal Dichalcogenides (TMDs), which have complementary properties to that of graphene. One major property is that they can have a large direct band gap, which graphene lacks. Lots of research is being done on combining graphene with TMDs in order to produce new, superior, electrical devices, such as high-speed transistors and sensors

Generally, graphene has been manufactured by mechanically cleaving it from much larger Highly Oriented Pyrolytic Graphite (HOPG) crystal by using mechanical exfoliation (also known as Scotch tape method). This method can produce pristine, very high-quality monocrystal graphene flakes on any substrate. Unfortunately, mechanical exfoliation is a slow and cumbersome process. It requires lots of manual work and ultimately produces only small graphene flakes; hardly the technique for industrial scale production. Another possibility is to use chemical exfoliation, which produces numerous graphene flakes that can be spin coated on a targeted substrate, but the graphene flakes are even smaller than with mechanical exfoliation and generally doped.

New methods for high throughput, large-scale production of graphene are being developed. Currently, the best candidate for this is Chemical Vapor Deposition (CVD), which can produce high-quality graphene over a large area on a selected catalytic substrates.

The same cumbersome mechanical exfoliation method used in manufacturing graphene is also applied with TMDs. The manufacturing of graphene-TMD heterostructures generally involves finding appropriate flakes after mechanical exfoliation, separating them from the substrate, aligning them and ultimately pressing them together, forming a graphene-TMD heterostructure. This process produces high-quality heterostructures, but it is very slow and requires manual work, and thus cannot be used in industrial scale production.

This thesis investigates whether it is possible to directly grow graphene via CVD on top, or under of, chemically exfoliated TMD nanoflakes. If successful, this manufacturing method would allow a quick production of a large number of graphene-TMD heterostructures with minimal manual work.

2 Background

2.1 Graphene

The name "graphene" was given to a two-dimensional (2-D) sheet of sp^2-hybridized carbon atoms that form a hexagonal lattice, also known as a honeycomb lattice, see Figure 1(a). Graphene sheets can be used to form other carbon allotropes; they can be rolled up to form 1-D carbon nanotubes, wrapped up to a 0-D fullerene structure or stacked to form 3-D graphite. Each carbon atom has four bonds, one π-bond pointing out-of-plane and three in-plane covalent σ-bonds at 120° angles binding carbon atoms together. The covalent σ-bonds are very strong and stable, giving arise to many physical properties of graphene. However, the electronic properties are due to a half-filled π-band, which is formed from overlapping π-bonds; this band allows free movement of electrons on the surface of graphene.

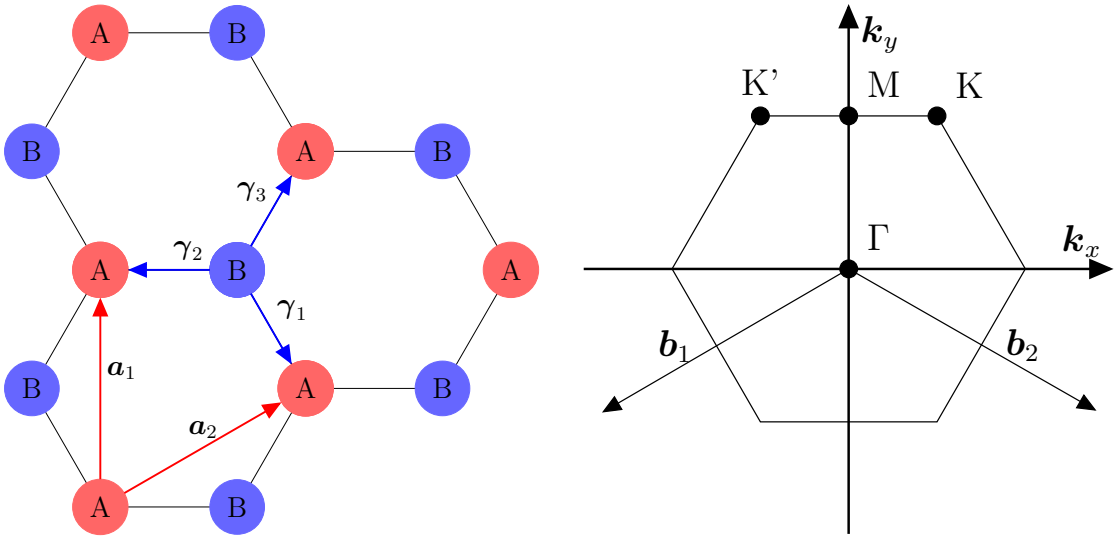

Figure 1: (a) Honeycomb lattice of graphene. The primitive unit cell consists of two carbon atoms, A and B, at K and K' –points of the Brillouin zone, respectively. Two lattice unit vectors $\boldsymbol{a}_1$ and $\boldsymbol{a}_2$ are shown in red and the nearest-neighbor vectors $\boldsymbol{\gamma}_1$, $\boldsymbol{\gamma}_2$ and $\boldsymbol{\gamma}_3$ in blue. (b) Brillouin zone of graphene, where a few symmetry points (K', K, M and Γ) are shown as well as reciprocal lattice vectors $\boldsymbol{b}_1$ and $\boldsymbol{b}_2$.

Graphene was the first 2-D material that was experimentally found to be stable in a free-standing form. Initial theoretical work by Peierls and Landau in the 1930s suggested that free-standing 2-D materials could not exist at any finite temperature [1]. The argument relied on the fact that atom displacement caused by thermal fluctuations is comparable to the interatomic distances and thus the crystal structure cannot be stable, i.e., long-wavelength fluctuations destroy long-range order. Even though the initial work used harmonic approximations and order-parameter expansions, later Mermin founded the argument to more rigorous grounds [2], where neither approximation was used.

In 1988 the theoretical foundation of Peierls and Landau was undermined by Nelson et al., who showed that while indeed 2-D crystals are not stable in 2-D space, they may be stable in 3-D space [3]. It was shown that a crumpling transition happens at a finite temperature, after which one cannot assume a pure 2-D crystal structure, but the third dimension must be accounted for. This transition would present itself as out-of-plane height fluctuations of the crystal.

In 2004 Geim and Novoselov succeeded to isolate monolayer graphene flakes on SiO_2/Si substrate from HOPG by means of mechanical exfoliation [4]. This was an experimental verification for the stability of 2-D materials, which could later be explained by assuming that the 2-D crystallites are in a metastable state due to being extracted from bulk 3-D material [1]. However, Monte Carlo simulations of graphene show that long-wavelength fluctuations (argument of Peierls and Landau) of the lattice are suppressed by anharmonic coupling between stretching and bending modes [5]. Furthermore, Scanning Tunneling Microscopy (STM) [6] and Transmission Electron Microscopy (TEM) [7] experiments of free-standing graphene show that it has intrinsic ripples on it, thereby corroborating the crumpling transition hypothesis given by Nelson et al.

One could also argue that the graphene layer on top of SiO_2/Si is no more than a part of a more rigid 3-D structure, hence not a true 2-D structure but merely quasi-two–dimensional. However, this is not the case as graphene is bound only by Van der Waals force to the substrate, in contrast to, e.g., SiGe on Si substrates grown by Molecular Beam Epitaxy (MBE). Furthermore, it is possible to manufacture a purely free-standing graphene layer.

2.1.1 Band structure

Bravais lattice (2-D) is defined as an infinite lattice generated by a set of discrete translations described by:

$$\boldsymbol{R}_n = n_1\boldsymbol{a}_1 + n_2\boldsymbol{a}_2, \text{ where } \quad \{n_1, n_2\} \in \mathbb{Z}. \tag{1}$$

We can use Bloch wave functions to describe this periodicity. A Bloch wave is defined as follows:

$$\Psi(\boldsymbol{r}) = \exp(i\boldsymbol{K}_m \cdot \boldsymbol{R}_n)u(\boldsymbol{r}), \text{ where } u(\boldsymbol{r}) = u(\boldsymbol{r} + \boldsymbol{R}_n). \tag{2}$$

Therefore by using argument of periodicity $\Psi(\boldsymbol{r}) = \Psi(\boldsymbol{r} + \boldsymbol{R}_n)$ we get

$$\exp(i\boldsymbol{K}_m \cdot (\boldsymbol{r} + \boldsymbol{R}_n))u(\boldsymbol{r} + \boldsymbol{R}_n) = \exp(i\boldsymbol{K}_m \cdot \boldsymbol{r})u(\boldsymbol{r}). \tag{3}$$

Next we use the fact that $u(\boldsymbol{r})$ is a periodic function with the same periodicity as $\Psi(\boldsymbol{r})$, i.e., $u(\boldsymbol{r}) = u(\boldsymbol{r} + \boldsymbol{R}_n)$ giving

$$\exp(i\boldsymbol{K}_m \cdot \boldsymbol{r}) \exp(i\boldsymbol{K}_m \cdot \boldsymbol{R}_n) = \exp(i\boldsymbol{K}_m \cdot \boldsymbol{r}), \tag{4}$$

thus it must be that

$$\exp(i\boldsymbol{K}_m \cdot \boldsymbol{R}_n) = 1 \;\rightarrow\; \boldsymbol{K}_m \cdot \boldsymbol{R}_n = 2\pi N, \text{ where } N \in \mathbb{Z}. \tag{5}$$

The reciprocal lattice is defined as set of vectors $\boldsymbol{K}_m = m_1\boldsymbol{b}_1 + m_2\boldsymbol{b}_2$, where $\{m_1, m_2\} \in \mathbb{Z}$ that satisfy the condition in Equation 5. One can determine the vectors $\boldsymbol{b}_1$ and $\boldsymbol{b}_2$ by means of vector algebra:

$$\boldsymbol{b}_1 = 2\pi\frac{-\bar{\boldsymbol{R}}\boldsymbol{a}_2}{-\boldsymbol{a}_1 \cdot \bar{\boldsymbol{R}}\boldsymbol{a}_2}, \quad \boldsymbol{b}_2 = 2\pi\frac{\bar{\boldsymbol{R}}\boldsymbol{a}_1}{\boldsymbol{a}_2 \cdot \bar{\boldsymbol{R}}\boldsymbol{a}_1}, \tag{6}$$

where $\bar{\boldsymbol{R}}$ is the 90-degree rotational matrix $\bar{\boldsymbol{R}} = \left(\begin{smallmatrix} 0 & -1 \\ 1 & 0 \end{smallmatrix}\right)$.

Graphene lattice is not a Bravais lattice due to the breaking of rotational symmetry between points A and B, see Figure 1(a). However, by considering it as a trigonal lattice with two atoms per unit cell (carbon atoms of K and K' –points of the Brillouin zone), it can be converted to a Bravais lattice. The lattice vectors of this system can be represented as:

$$\boldsymbol{a}_1 = \frac{a_0}{2}\begin{bmatrix} 3 \\ \sqrt{3} \end{bmatrix}, \quad \boldsymbol{a}_2 = \frac{a_0}{2}\begin{bmatrix} 3 \\ -\sqrt{3} \end{bmatrix}, \tag{7}$$

where $a_0 \approx 1.42$ Å is the carbon-carbon distance. By utilizing Equation 6 we get the reciprocal vectors seen in Figure 1(b)

$$\boldsymbol{b}_1 = \frac{2\pi}{3a_0}\begin{bmatrix} 1 \\ \sqrt{3} \end{bmatrix}, \quad \boldsymbol{b}_2 = \frac{2\pi}{3a_0}\begin{bmatrix} 1 \\ -\sqrt{3} \end{bmatrix}. \tag{8}$$

Dispersion relation $E_\pm(\boldsymbol{k})$ can be calculated with nearest-neighbor tight-binding model (described elsewhere [8]), giving:

$$E_\pm(\boldsymbol{k}) = \pm t\sqrt{3 + f(\boldsymbol{k})} - t'f(\boldsymbol{k}), \text{ where} \tag{9}$$

$$f(\boldsymbol{k}) = 2\cos\left(k_y a_0\sqrt{3}\right) + 4\cos\left(k_y a_0\frac{\sqrt{3}}{2}\right)\cos\left(k_x a_0\frac{3}{2}\right). \tag{10}$$

Here $t \approx 2.8$ eV is the nearest-neighbor hopping energy, and t' is the next nearest-neighbor hopping energy. The result of Equations 9 and 10 is shown in Figure 2, where the next nearest-neighbors are disregarded ($t' = 0$).

Due to its peculiar band structure graphene can be categorized as a zero band gap semiconductor or a semimetal. It has *Dirac cones* in its valence and conduction bands that meet at the K and K' –points of the Brillouin zone, see Figures 2 and 1(b). Therefore graphene has no band gap, and due to the Dirac cones touching only at a single point, it is not a metal either. Interestingly, instead of the normal parabolic dispersion relation, Dirac cones have a *linear* dispersion relation near the K and K' –points. This linear relation means that the Hamiltonian for describing electrons in graphene has the same form as massless Dirac fermions in relativistic Schrödinger's equations (i.e., Dirac equations)[1]. That is why electrons in graphene are sometimes referred to as being massless.

2.1.2 Properties and devices

Graphene has many unique properties that supersede that of many bulk materials. It has extremely high electron mobility (2×10^5 cm^{2}V^{-1}s^{-1}) [9] and thermal conductivity

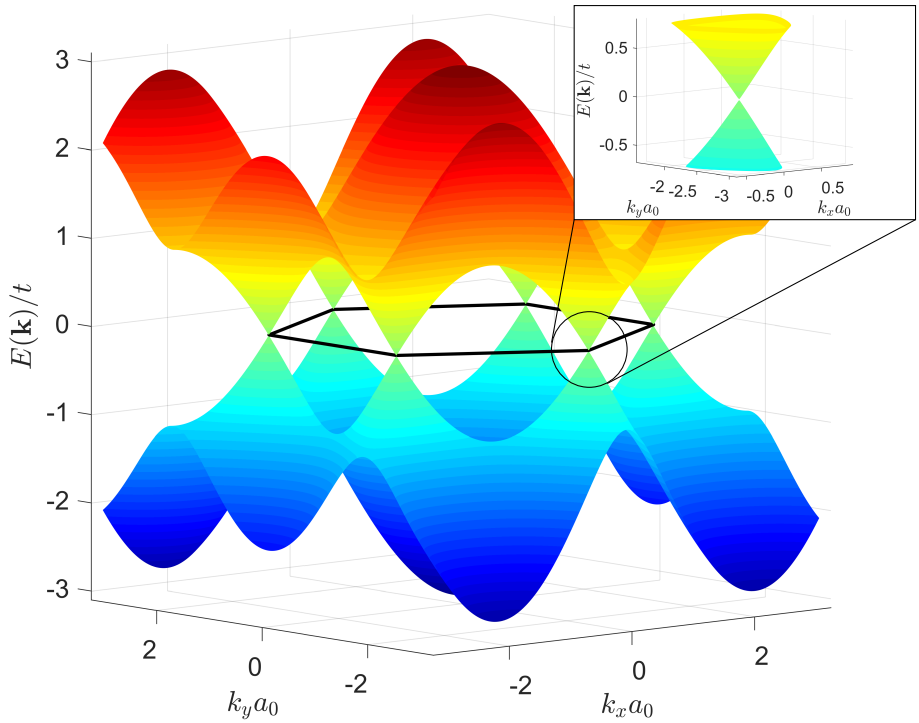

Figure 2: Graphene band structure using nearest neighbors tight binding model. The conduction band (red) and valence band (blue) meet at K and K' –points of Brillouin zone. The contact points look like two touching cones (Dirac cones) at the corners of the black hexagon (depicting reciprocal lattice of graphene, see Figure 1(b)).

(up to 5.3×10^3 $\mathrm{Wm^{-1}K^{-1}}$) [10] in room temperatures. Being 2-D in nature makes it flexible and stretchable as well as transparent (monolayer graphene absorbs only 2.3 % of the visible spectrum [11]). Graphene is extremely strong: it has Young's modulus of 1 TPa and ultimate tensile strength of 130 GPa [12]. In addition, graphene is also impermeable to gases [13] and exhibits interesting quantum properties, such as room-temperature quantum Hall effect [14, 15] and anomalous quantum Hall effect (theoretical work) [16].

The absence of band gap (see Section 2.1.1) means that graphene-based Field Effect Transistors (FETs) lose the ability to be switched off, one of the key properties of Complementary Metal-Oxide–Semiconductor (CMOS) devices. However, in radio frequency applications switching off is not necessarily needed because the transistor works as an amplifier that is constantly on. Standard top-gated graphene FETs have achieved cut-off frequencies (f_T) of 100 GHz [17] and novel nanowire (NW) gate FETs up to 300 GHz [18], both reaching the Extremely High Frequency (EHF) regime. State-of-the-art Indium Phosphide (InP) High Electron Mobility Transistor (HEMTs) have already reached unity power gain frequencies (f_max) up to 1 THz with $f_\mathrm{T} = 610$ GHz [19, 20]. Unfortunately they require sophisticated epitaxial growth methods and are not compatible with flexible electronics. Flexible graphene FETs can reach strains up to 8 %, with $f_\mathrm{max} = 2.1$ GHz and $f_\mathrm{T} = 25$ GHz [21], and by using smaller channel length frequencies up to $f_\mathrm{max} = 7.6$ GHz and $f_\mathrm{T} = 38.7$ GHz at 2 % strain are possible

[22]. In comparison, using self-sustained straining approach, single-crystalline Si/SiGe nanomembranes (NM) can reach strains up to 1 % while having $f_{\max} = 15.1$ GHz and $f_{\mathrm{T}} = 5.1$ GHz [23]. Accepting even less strain (∼0.25 %), InAs compound semiconductor-on-insulator (XOI) FETs can achieve values of $f_{\max} = 22.9$ GHz and $f_{\mathrm{T}} = 105.0$ GHz [24]. It should be noted that the references where $f_{\max} = 1$ THz and $f_{\mathrm{T}} = 610$ GHz were reached (references [19] and [20]), a technique called "on-wafer-calibration" was used for removing parasitic resistances, instead of de-embedding, which has been used in the other articles in this paragraph, making real comparisons challenging. All of the different transistors mentioned in this paragraph are compiled in Table 1.

Table 1: Comparison of group IV and III-V transistors to graphene-based.

Type	**Material**	**Strain**	$\mathbf{f_{max}}$	$\mathbf{f_T}$	**Ref**
Top gate FET	graphene	-	10 GHz	100 GHz	[17]
Top gate NW FET	Co_2Si NW and graphene	-	2.4 GHz	300 GHz	[18]
HEMT	InP	-	1 THz*	610 GHz*	[19, 20]
Bottom gate FET	graphene	8 %	2.1 GHz	25 GHz	[21]
Bottom gate FET	graphene	2 %	7.6 GHz	38.7 GHz	[22]
Top gate FET	Si/SiGe NM	1 %	5.1 GHz	15.1 GHz	[23]
XOI FET	InAs	0.25 %	22.9 GHz	105.0 GHz	[24]

* On-wafer-calibration used instead of de-embedding for removal of parasitic resistances.

Even though monolayer graphene has no intrinsic band gap, it is possible to open a band gap retroactively. An early theoretical study suggested that a very small band gap of ∼53 meV can be opened by placing monolayer graphene on a hexagonal Boron Nitride (hBN) substrate, due to a breaking of sublattice symmetry [25]. However, no later physical experiments have found such band gap opening [26]. Still, a band gap of ∼200 meV can be opened by using graphene nanoribbons as narrow as ∼15 nm [27]. Another possibility to open a band gap is to use gated bilayer graphene, which opens up a tunable band gap in the range of 0–250 meV [28]. However, these retroactively opened graphene band gaps are quite small in comparison to, e.g., intrinsic Si band gap of 1.12 eV [29].

2.1.3 Fabrication

The standard way of producing pristine graphene flakes is by means of mechanical exfoliation, also called the Scotch tape method. In this method, small graphene flakes (or flakes of any layered material, that is, a material where the molecular layers are bound by Van der Waals force) can be placed on a substrate by repeatedly thinning bulk graphite (HOPG) flake. A small piece of graphite is placed on a sticky tape, which is repeatedly folded over and released to spread graphite on the tape. After this process has been repeated numerous times the sticky tape can be pressed against a substrate (generally SiO_2/Si substrate) and then torn off. Some of the

thin graphite flakes are transferred on the substrate. In this process a very small portion of them have a thickness of only one atomic layer, resulting in the desired graphene flakes on the substrate. See Section 3.2 for more detailed description using hBN as a source. Generally, the lateral sizes of the acquired flakes are in the tens of micrometers range, but hundreds of microns are possible.

In order for commercial devices to be able to exploit any of graphene's properties, there should be an economically feasible, high-quality, large-area graphene synthesis process available. Early large-area graphene synthesis focused on Silicon Carbide (SiC) substrates as a graphene source. The silicon atoms are sublimated from the crystal surface exposing a layer of graphene. However, SiC substrates are very expensive and the sublimation of silicon atoms needs temperatures of ∼1650 °C at 900 mbar [30]. At slightly lower temperatures of ∼1280 °C ultra-high vacuum (UHV) is required [31]. High temperatures and UHV conditions increase the cost of this method even further and make it hard to integrate this technology with other substrates and materials. Furthermore, this method produces terrace like graphene structures due to small wafer cutting angle misalignment [32]; therefore, no smooth and continuous wafer wide graphene layer is accomplished.

Chemical exfoliation is a top-down method that can also be used. In this method, a graphite sample is agitated in a chemical solution where certain molecules, such as N-methyl-pyrrolidone (NPM) [33], can intercalate between graphite layers, thereby separating and thinning them down into very thin layers. Another top-down method is by reduction of graphene oxide. Unfortunately, the resulting graphene layer in both methods is more of a mix of thinner and thicker flakes, with sub-par quality and small flake size. [34]

The most promising alternative to aforementioned top-down methods is Chemical Vapor Deposition (CVD), which is inherently a bottom-up method. It is based on catalytic pyrolysis of hydrocarbon precursors, which will produce carbon species that are able to adsorb on a selected substrate and ultimately bond together, forming graphene. CVD can be used to grow large area graphene on many catalytic substrates, see Section 2.3 for general CVD and specifically for graphene CVD see section 2.3.1.

2.2 Transition Metal Dichalcogenides

Transition Metal Dichalcogenides (TMDs) are layered compounds with a generalized chemical formula of MX_2, where M stands for transition metal (generally recognized as groups 4–11 of the periodic table with few modifications) and X for a chalcogenide (group 16, also known as oxygen family). TMDs form layered structures with two chalcogenide lattices separated by one metal lattice, see Figure 3 for an example of one possible polymorph. The overall symmetry is trigonal, hexagonal or rhombohedral for bulk [35], but with monolayers only trigonal and hexagonal polymorphs are possible.

2.2.1 Properties

TMDs have gained much attention after the discovery of graphene because they exhibit complementary properties to those of graphene. Even though graphene has

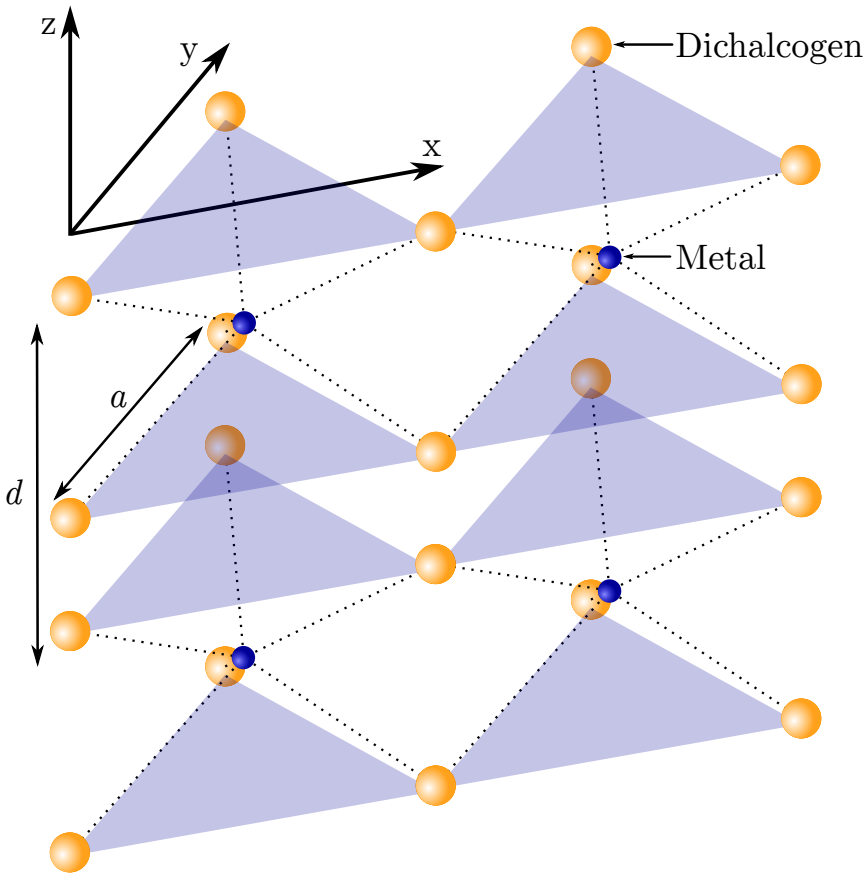

Figure 3: Trigonal prismatic lattice with one layer per repeat unit (A b A stacking, where dichalcogenide layers and the metal layer are represented by capital, and non-capital letters, respectively): a possible TMD lattice structure. The distance between repeating units is given by d and lattice constant is given by a. The top-down image of this particular TMD structure is the same as in Figure 1(a), but with A and B replaced with metal and dichalcogenide atoms, respectively. Another geometrical possibility would be hexagonal polymorph, where the stacking order is A b C, with one dichalcogenide layer mirrored over the x-axis, hence it is also referred to as trigonal anti-prismatic lattice.

shown excellent properties (see Section 2.1) and has many potential applications, it still remains chemically inert and has no native band gap. Due to the lack of a band gap, e.g., FETs with high on/off ratios cannot be manufactured. In contrast, TMDs are chemically active, have a wide range of band gaps and mobilities [36]. Furthermore, they can be mechanically exfoliated because they have strong in-plane covalent/ionic bonding and weak Van der Waals bonding out-of-plane.

Some TMDs, such as $TiSe_2$, have interesting low-temperature properties, e.g.,

- superconductivity,
- charge density waves (periodic deformation of the crystal structure) and
- Mott phase transition (conductive to non-conductive transition not explained

by conventional band theory) [37].

Group 6 TMDs exhibit spin and valley polarization [38]. The valley quantum number of an electron in a lattice depends on the electron's momentum. Should an electron reside in a "valley" of the conduction band (the dispersion relation of a conduction band looks as if it has numerous "valleys" in it, hence the name, see Figure 2) it has different valley quantum number. Therefore, by controlling valley degree of freedom it is possible to encode information into the valley quantum number. The concept of storing information into the electron spin degree of freedom is called spintronics, thus storing information into valley polarization has been dubbed as valleytronics.

2.2.2 Fabrication

All MoX_2 and WX_2 compounds are predicted to undergo a gradual transition from indirect band gap material to direct band gap, as the thickness goes toward monolayer [35], therefore generally mechanical exfoliation is used to obtain large monolayer TMD samples, see Section 3.2 for more details.

Standard liquid exfoliation techniques can be used if monolayer yield nor flake size is of no importance. A more specific liquid exfoliation technique, ultrasound-promoted hydration by lithium-intercalated compounds, can produce nearly 100 % monolayer yield with lateral sizes up to 1 µm [39, 40]. Even though the yield and density are high, the size of the flakes is still much less than with mechanical exfoliation.

TMDs can also be grown with CVD (see Section 2.3). MoS_2 and MSe_2 have been the most used TMDs for CVD growth and there are four generally accepted methods for growing these TMDs:

(i) Decomposition of metal and dichalcogenide precursors (gas phase [41, 42] or dip-coated [43]), followed by deposition of TMDs.

(ii) Chalcogenization of a metal film [44].

(iii) Direct conversion of metal oxide to metal dichalcogenide by selenization or sulfurization [45].

(iv) Gas phase transport and recrystallization of TMD powders on arbitrary substrates [46].

Unfortunately precise thickness control and uniformity are hard to achieve with the aforementioned methods as they depend on precursor concentrations and substrate pretreatments (instead of any inherent mechanism that facilitates uniform monolayer growth, e.g., surface catalytic growth).

2.3 Chemical vapor deposition

Chemical Vapor Deposition (CVD) is a technique that exploits the tendency for materials to go through chemical reactions at elevated temperatures. It is possible

to inject precursor gases into a heated chamber where they combine to form a new molecule which is then absorbed on a selected surface. Usually, the process is done in vacuum conditions but atmospheric pressure CVD is also possible. For example, coating silicon with silicon dioxide can be done with CVD (atmospheric or vacuum), where silane and oxygen are injected into the system. The silane goes through pyrolysis in the gas phase and decomposes into silicon and hydrogen. The silicon gas combines with oxygen to form silicon dioxide, which then adsorbs on a silicon wafer. Other compounds instead of silane can also be used.

There are many different types of CVD processes which generally are differentiated by four categories:

- **Pressure:** Often anything between Ultra-High Vacuum (UHV) and atmospheric are used, where the low-pressure regime is the most common. High-pressure CVD is also possible but is rarely used.
- **Heating:** There are two main types of heating systems in CVD. In hot-wall CVD the entire chamber is heated, usually with external heating coils. Conversely, in cold-wall CVD only specific parts are heated, such as the substrate and the showerhead. See Figure 4 for examples of these. It is also possible to use Plasma Enhanced CVD (PECVD), where AC or DC plasma is used to assist the disassociation of molecules in the chamber, allowing lower deposition temperatures.
- **Precursor:** Typically the precursor is merely a gas, but liquid or a combination of both (an aerosol) or a solid can also be used. In Metal-Organic CVD (MOCVD) the precursor is an organometallic compound, meaning that it has at least one bond between an organic compound and a metal. Usually the precursors and disassociated compounds of an MOCVD system are highly toxic.
- **Geometry:** Two different geometries exist for CVD, vertical and horizontal. Generally, hot-wall systems have horizontal geometries, where the gases flow laterally over the sample. In vertical systems the gases are injected through a showerhead directly towards the sample. Vertical geometry can translate into a better conformity of growth as precursor gases are spread evenly throughout the sample; vertical systems are usually of cold-wall design, see Figure 4.

2.3.1 Graphene via CVD

When fabricating graphene with CVD catalytic pyrolysis of carbon containing precursor is generally used to reduce the needed growth temperature. Catalytic properties of transition metals are well known and arise from their partly filled d-orbitals. Graphene has been grown on numerous transition metals, such as copper [47], ruthenium (Ru) [48], nickel (Ni) [49], platinum (Pt) [50], iridium (Ir) [51] and palladium (Pd) [52]. The carbon precursor is often methane, but other possibilities exist, e.g., acetylene or ethylene. Solid precursors can also be used, for example, Polymethyl

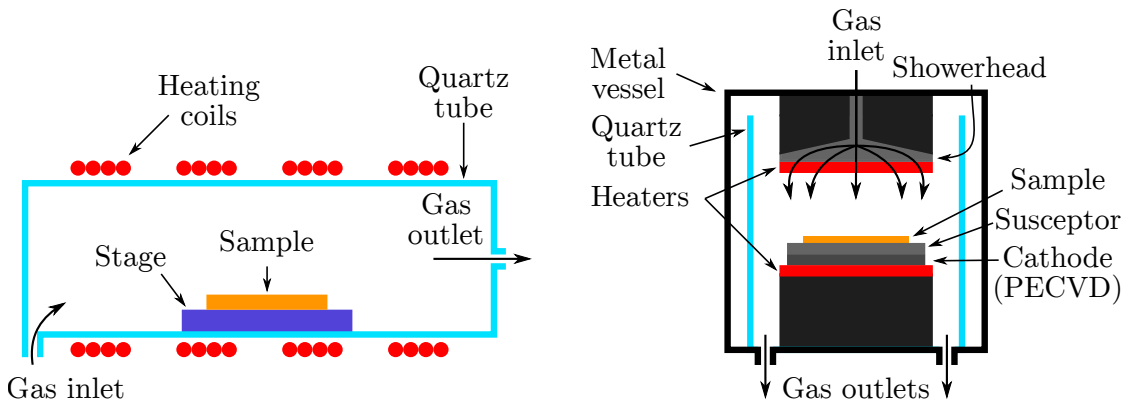

Figure 4: (a) Horizontal CVD furnace with a hot-wall design. Heating coils heat up the quartz tube which in turn heats up the sample through conduction and convection. (b) Vertical CVD furnace with a cold-wall design. The top heater heats up the gases, which are injected through the showerhead while the bottom heater heats up the sample directly.

methacrylate (PMMA) [53]. Even more exotic precursors, such as food or roach legs can be used [54]. In fact it seems to be possible to use any hydrocarbon to grow graphene, however the quality may suffer.

Graphene growth in CVD is usually is done in the presence of three different gases: carbon precursor, carrier gas, and a reducing agent. For example a combination of methane as a precursor, argon as carrier gas and hydrogen as a reducing agent could be used. Generally the four steps to any CVD graphene process are:

- **Pre-heating:** The chamber and gases (hot-wall reactor) or only the substrate (cold-wall reactor) are heated up to a specific temperature.
- **Annealing:** The substrate surface is reduced by, e.g., hydrogen which cleans the catalytic surface. High temperatures (∼1000 °C) and long annealing times ($>$ 30 min) can be used to decrease the surface roughness, change crystal orientation to a more convenient one and increase the grain size.
- **Growing:** Carbon-containing precursor is injected into the reactor. Generally accompanied by a reducing agent and a carrier gas. Parameters, such as temperature, total pressure, partial pressures of gases and growth time can be changed to optimize the resulting graphene quality. It is possible to use multi-step growth processes but often only a one-step process is used.
- **Cooling:** This is usually done in an inert atmosphere. Graphene can oxidize at temperatures of ∼150 °C, thus the chamber temperature needs to be below this before samples can be brought to normal atmosphere. Should graphene growth be done via a precipitation mechanism (see Section 2.3.2), the cooling step is *crucial* if one wants to get as thin graphene as possible.

Even though CVD can produce large area graphene, there are still several problems with the technique. The quality of continuous CVD graphene has not yet reached

the level of mechanically exfoliated graphene. Continuous CVD graphene has, for example, greater amount of defects, problems with impurity doping [55, 56] and much lower carrier mobility [50, 57, 58]. However, non-continuous monocrystalline CVD graphene (i.e., graphene flakes) can have as good carrier mobility as mechanically exfoliated flakes [59, 60]. Non-continuous graphene is grown with low methane flow in order to reduce a number of nucleation sites. These sparsely scattered nucleations sites can grow up to millimeter scale [61, 62]. However, this is done by sacrificing growth speed (several hours of growth time instead of minutes) and the result is only flakes instead of a one continuous graphene layer. Fast growth and continuous layer are both some of they key points of CVD and extremely important features for the industry.

Many substrates, such as copper exhibit only weak interaction between the substrate and the graphene layer resulting in polycrystalline graphene. This introduces scattering due to grain boundaries, which diminishes the properties of graphene. In mechanically exfoliated graphene the sheet is sometimes monocrystalline – there are no scattering effects from grain boundaries.

When using strongly interacting substrates, such as nickel, it is possible to grow monocrystalline graphene due to stronger interaction and small lattice mismatch [63]. Unfortunately many of these substrates have high carbon solubility resulting in difficulties with monolayer graphene growth due to the precipitation mechanism (see Section 2.3.2). Furthermore, even though growing monocrystalline graphene on nickel is possible, Density Functional Theory (DFT) calculations and STM measurements show that there are two preferred translations in relation to the substrate for graphene domains on nickel [64]. Thus it is questionable whether the result can be truly said to be monocrystalline.

2.3.2 Growth dynamics

In general, there are seven steps that the carbon precursor can go through in a graphene growth process:

- gas phase pyrolysis,
- adsorption,
- catalytic pyrolysis,
- migration,
- bulk diffusion,
- nucleation (growth),
- precipitation.

See Figure 5 for an illustration of these steps. Firstly the carbon precursor may go through pyrolysis in the bulk of the gas. This is undesired because the initial gas-phase pyrolysis reaction triggers an avalanche effect of subsequent chemical

reactions, resulting in soot. It is an extremely blackening substance, requiring no catalytic substrate, thus it can contaminate already formed graphene layers with amorphous carbon or with subsequent graphene layers. [65]

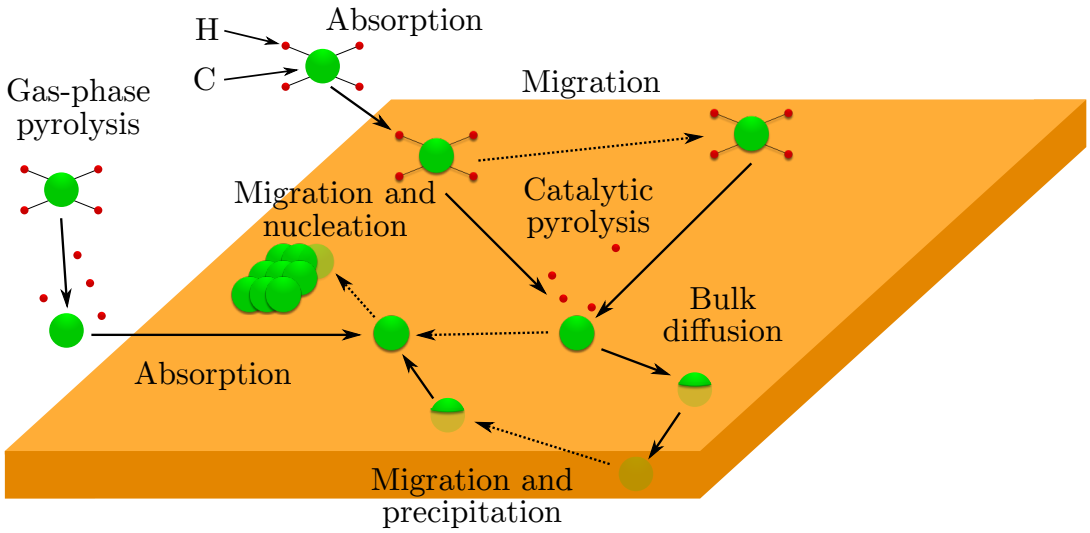

Figure 5: Simplified graphene growth steps in a CVD process. In this example methane is used as a carbon precursor. Notice that bulk diffusion and precipitation are not universal to all substrates; graphene on copper does not grow by precipitation mechanism, but by pure surface catalytic process, because the carbon solubility to copper is negligible. Adsorption after gas-phase pyrolysis can happen on virtually any place of the substrate, including on top of already formed graphene, contaminating it with amorphous carbon or with subsequent graphene layers.

Fortunately the dehydrogenation energies required for gas-phase pyrolysis of methane are relatively high: 4.85 eV, 5.13 eV, 4.93 eV, 3.72 eV for CH_3-H, CH_2-H, CH−H, C−H, respectively [66]. This translates into negligible gas-phase pyrolysis rates in low-pressure CVD using temperatures of ∼1000 °C, assuming effective gas residence times of $\tau_{eff} < 100$s and pure methane [67]. For example, the effective residence time τ_{eff} in a 6" vertical CVD apparatus (Aixtron Black Magic 6") with 1500 sccm of flow is only $t_{eff} = \sim 2$ s. The complete residence time can be calculated by

$$\tau = VT_0P/QTP_0, \tag{11}$$

where T_0 and P_0 are the ambient temperature and pressure; T and P are the temperature and pressure of the furnace; Q is the total gas flow and V is the total volume of the furnace [68]. Because the aforementioned equation relies on laminar flow, we can calculate the effective residence time:

$$\tau_{eff} = V_{eff}T_0P/QTP_0, \tag{12}$$

which is the time carbon precursor can go through pyrolysis and still contaminate the substrate. Here V_{eff} is the volume of the furnace upstream from the substrate, i.e., the volume between the sample and the showerhead in Figure 4(b).

Unfortunately decreasing methane partial pressure (using a gas mixture instead of pure methane) has the tendency to increase the amount of gas-phase pyrolysis in equilibrium and in non-equilibrium conditions [67]. This means that in very low methane partial pressures one can no longer assume gas-phase pyrolysis to be negligible. This effect is intensified even further by introducing hydrogen into the gas mixture [69]. The gas-phase pyrolysis can happen at such a rate that it has to be minimized before good quality graphene can be grown [65]. Should other carbon precursors be used, such as acetylene or ethylene, the growth temperatures can be reduced. However, because methane is the most stable hydrocarbon up to ∼1000 °C [69], the reduction of growth temperature with a non-methane precursor will increase the rate of gas-phase pyrolysis.

As was mentioned in Section 2.3.1, the catalytic properties of transition metals are well known. For example, in the case of copper, the activation energies of methane dehydrogenation ($CH_x \rightarrow CH_{x-1} + H,\ x = \{4, 3, 2, 1\}$) are reduced considerably, from 3.23–4.66 eV [70] to 1.12–1.86 eV due to the formation of strong bonds on copper (Cu) surfaces, such as $Cu{-}CH_x,\ x = \{4, 3, 2, 1\}$ and Cu−H. Also the total dehydrogenation ($CH_4 \rightarrow C + 4H$) energy is reduced from 18.63 eV to 6.44 eV. [66] This large activation energy reduction in combination with virtually zero carbon solubility makes copper an excellent substrate for graphene growth. Even though the activation energies for dehydrogenation are considerably lower on copper than in the gas-phase, many other transition metals reduce it even further, e.g., Ru reduces it down to 0.62–1.19 eV and Pd to 0.79–1.02 eV [66].

Even though total dehydrogenation ($CH_x \rightarrow C + xH$) was discussed and shown in Figure 5, the complete graphene formation process on a catalytic substrate is much more complex. For starters, the amount of molecular hydrogen in the gas mixture changes the growth process because hydrogen contests with methane over active surface sites, inhibiting the surface catalytic process of methane. Furthermore, hydrogen adsorption activation energy on copper is only ∼0.20 eV [71] while it is ∼2 eV [72] for methane, meaning that hydrogen adsorbs on copper much more easily.

Oftentimes hydrogen is introduced during the annealing phase to remove native oxides from the copper surface; this saturates the substrate with hydrogen even prior to methane injection. In addition, hydrogen acts as an etchant for graphene at high-temperatures, thus it serves a dual purpose: inhibiting graphene formation by using active surface sites and by etching already formed graphene. However, the complete role of hydrogen is still under debate, as hydrogen seems to *promote* graphene growth to such an effect that a critical hydrogen concentration point can be found, prior to which graphene growth is very minimal [73, 74, 75]. Nonetheless, very large size graphene flakes can be grown *without* the use of hydrogen in any of the graphene growth steps [76].

Here a more detailed explanation of graphene growth on copper substrates is given; however, it should be noted that the complete process of graphene growth on copper (or on any substrate) is under debate and no general consensus exists. During the growth process methane is adsorbed on the surface, where dehydrogenation is probable up to CH_2, thus $CH_4 \rightarrow CH_3 + H$ or $CH_3 \rightarrow CH_2 + H$ are probable, or in short $CH_x \rightarrow CH_{x-1} + H,\ x = \{4, 3\}$. It should be noted, that even though the

reactions are probable, this is still the rate limiting step for the whole graphene formation process. The resulting monomer CH_{x-1} from methane dehydrogenation goes through migration phase until it meets another monomer. At this point they form a dimer $CH_{x-1} + CH_y \rightarrow C_2H_z + nH$ and another dehydrogenation occurs. The carbon dimer C_2H_z is very unstable on a copper surface, thus desorption or decomposition occurs fast, so it is probable that $z = 0$. Now two dimers can polymerize $C_2H_z + C_2H_i \rightarrow C_4H_{z+i}$ and further incorporate a third dimer to aromatize $C_4H_{z+i} + C_2H_k \rightarrow C_6H_{z+i+k}$. Notice that due to the unstable nature of the dimer $C_2H_{\{z,t,k\}}$ on copper it is probable that the aromatic hydrocarbon C_6H_{z+i+k} has $z = i = k = 0$, thereby the unstable dimer should be considered the first carbon deposit on the copper. This is not a unique route to total aromatization of carbon, but it is a probable one. The growth of graphene domain continues from the formed aromatic ring. A new dimer is formed by one of the monomers of the aromatic ring and by one extra monomer, thereby starting the growth of another aromatic ring next to the first one. [77] The effect of this type of a growth can be seen by isotope labeling where methane with C^{12} and methane with C^{13} are injected into the system periodically; one can see that rings of graphene are formed around the initial nucleation site [78]. The complete process has been gathered in Equations (13)–(16) and an illustration of a possible catalytic process for methane on a copper substrate in is given in Figure 6.

Catalytic dehydrogenation:	$CH_x \rightarrow CH_{x-1} + H,\ x = \{4, 3\}$	(13)
Dimer formation:	$CH_{x-1} + CH_y \rightarrow C_2H_z + nH$	(14)
Polymerization:	$C_2H_z + C_2H_i \rightarrow C_4H_{z+i}$	(15)
Aromatization:	$C_4H_{z+i} + C_2H_k \rightarrow C_6H_{z+i+k}$	(16)

During the early days of graphene CVD controlled precipitation of carbon was used to manufacture thin layers of graphene. The disassociated carbon at high-temperatures is absorbed into the bulk of a catalyst, thereby inhibiting graphene growth on the surface. As the catalyst cools down, the carbon precipitates to the surface and forms graphene. It is known that the bulk solubility of carbon to many transition metals can be controlled via temperature [79, 80]. Few layer graphene islands were fabricated utilizing this method on (0001) ruthenium in 2008 [48] and ∼10 layer continuous graphene films on nickel in the same year [49]. Later it was found out that copper has virtually zero carbon solubility, which then was used to directly grow graphene on a copper substrate by surface catalytic process [47], without the need to control the precipitation rate. The pure surface catalytic process also has the advantage of being self-limiting: when the first graphene layer is complete no additional layers are formed due to no exposed surface area of copper to the carbon precursor. This is also known as catalyst poisoning. The observation of pure surface catalytic growth initiated a wide use of copper as a catalyst for graphene growth and nowadays it is the most used substrate for CVD graphene.

Even though copper provides an intrinsically self-limiting substrate, in reality, more than one layer can be formed on the catalyst; this is due to the catalyst not being ideal. Commercial copper foils are often used in graphene synthesis and these

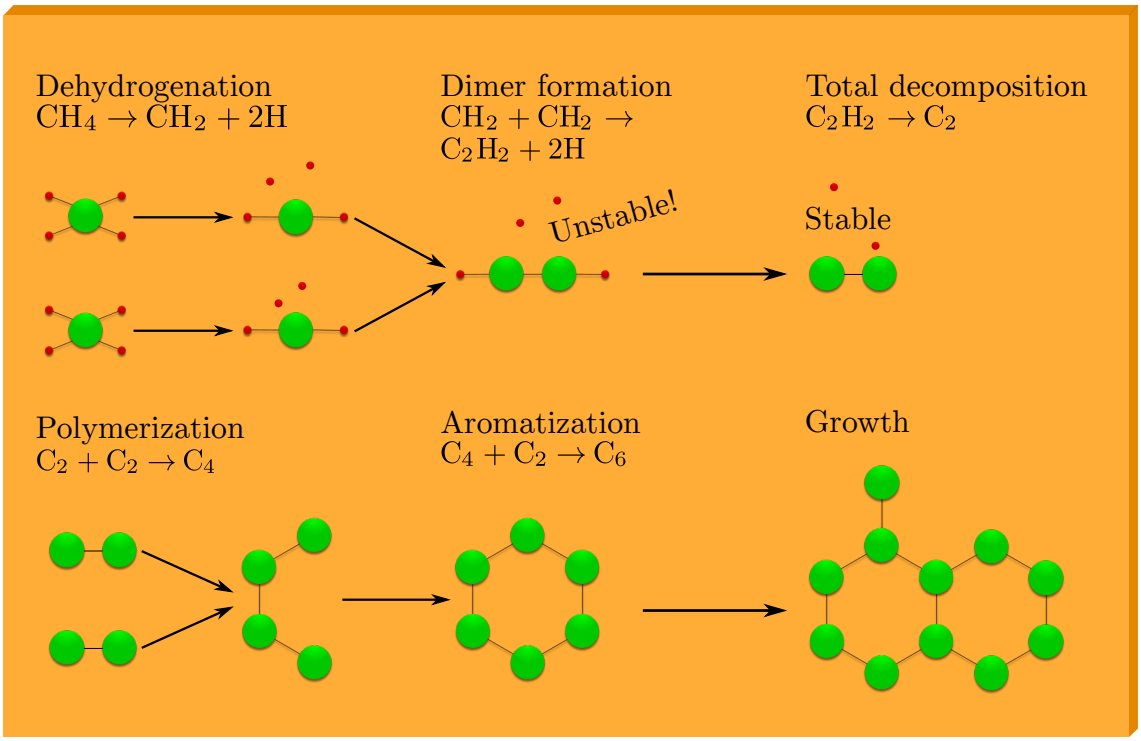

Figure 6: A possible route for graphene formation via surface catalytic pyrolysis of methane. Methane adsorbs on the substrate, where dehydrogenation occurs. The resulting monomer binds together with another monomer forming an unstable dimer. This unstable dimer goes through another dehydrogenation resulting in a stable dimer, which binds together with another dimer and finally aromatization occurs. Graphene crystal starts to grow from the formed aromatic ring.

foils are not atomically smooth. They have lots of micro- and macro-scale variations in roughness because they are manufactured by a rolling mill method, which leaves deep and long striations on the foil. Furthermore, the foils are not polished in any way, thus high micro-scale roughness exists as well. Topological imperfections are not the only type of imperfections present in commercial copper foils, they can have many impurity particles from the manufacturing process [81], and more can be introduced by the CVD process itself [82]. All of these imperfections (contaminants and surface irregularities) act as nucleation sites for initial graphene formation and for multilayer graphene flakes [83]. See Figure 7 for Scanning Electron Microscope (SEM) image of CVD graphene grown on copper and transferred to a SiO_2/Si substrate.

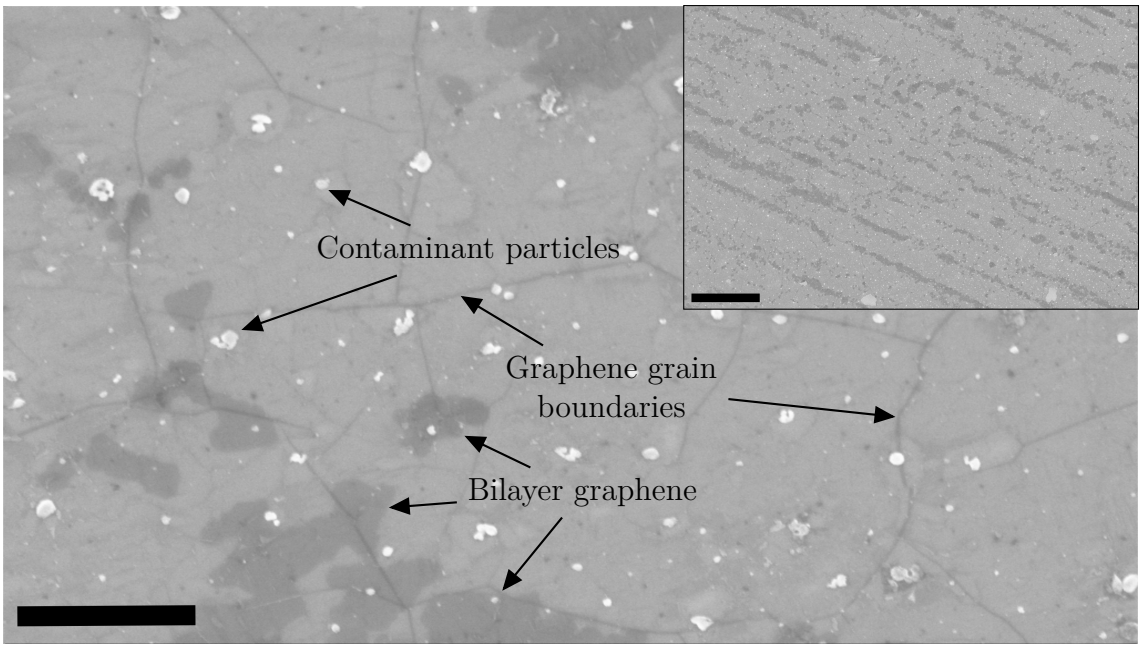

Figure 7: SEM image of CVD graphene transferred on a SiO_2/Si chip. White particles are contaminants from the copper foil or from the CVD process itself, e.g., silica particles from quartz parts [82]. Bilayer graphene flakes are shown in darker regions. Inset: Low magnification image from the same position, here it can be seen that bilayer graphene is primarily formed in stripes; in fact, they are mainly formed on the striations of the copper foil from the manufacturing process. Scale bars: 2 µm and 20 µm for inset.

2.3.3 Growth on TMDs

A few different routes for graphene growth on top or under of TMD nanoflakes can be speculated from what has been discussed in the Section 2.3. Essentially, three different routes are possible:

- **Precipitation:** Absorbed atomic carbon precipitates from the bulk substrate to surface sites which are already covered by a TMD flake. Therefore, the graphene would grow in between the TMD flake and the substrate.
- **Catalytic transparency:** The thin TMD flake does not fully prevent the catalytic effects of the substrate, thus graphene can grow on the TMD flake through normal catalytic growth [59]. Consequently, graphene would grow on top of the TMD flake.
- **Intercalation:** Adsorbed atomic carbon migrates in between the TMD flake and the substrate via intercalation due to the weak Van der Waals interaction of the substrate and the TMD flake. Hence, graphene would grow in between the TMD flake and the substrate.

The precipitation mechanism is non-existent in copper, due to very low carbon solubility. Therefore, catalytic transparency or intercalation are the two possible

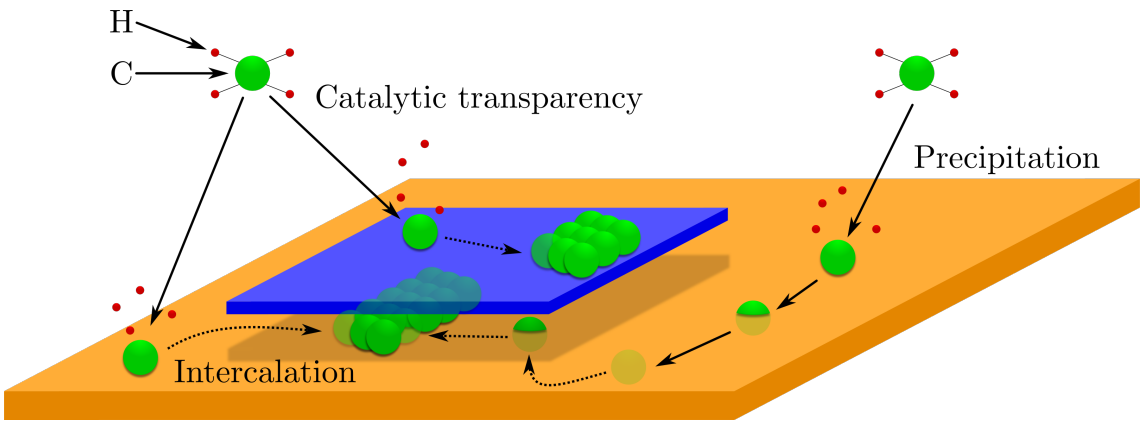

Figure 8: Possible growth mechanisms of CVD graphene on top or under of TMD nanoflakes. Blue represents TMD flake and orange is a catalytic substrate. The shadowed region represents Van der Waals force between the substrate and the TMD flake. Catalytic transparency: the TMD flake does not fully prevent the catalytic effects of the substrate. Hence, pyrolysis on the TMD flake can happen and growth continues as without the flake. Intercalation: catalytic pyrolysis happens on the substrate, after which the adsorbed carbon intercalates between the substrate and the TMD flake. Precipitation: after catalytic pyrolysis the atomic carbon diffuses into the bulk of the substrate. After a migration period it surfaces under the TMD flake.

routes for graphene growth. This is fortunate because the two routes can be distinguished merely by analyzing whether graphene grows on top of or under of TMD nanoflakes.

3 Methods

3.1 TMD nanoflakes

Three different TMD nanoflakes were used in this study: Tungsten Disulfide (WS_2), Molybdenum Disulfide (MoS_2) and hexagonal Boron Nitride (hBN). All three types of nanoflakes were bought from Graphene Supermarket (item codes: WS2-100ML, MOS2-100ML and BN-100ML, for WS_2, MoS_2 and hBN, respectively). The nanoflakes were all suspended in ethanol-water solution (45:55 for WS_2 and MoS_2, 50:50 for hBN). Dimensions specified by Graphene Supermarket (diameter and number of monolayers) of the different TMD flakes were as follows: MoS_2 100–400 nm (1–8 monolayers), WS_2 50–150 nm (1–4 monolayers) and hBN 20–200 nm (1–5 monolayers).

Spin coating (2000 1/min for 30 s) was used to disperse the nanoflake solutions on a 6" copper foils measuring 25 µm in thickness. For small area deposition, a droplet of nanoflake solution was applied on the substrate and thorough wetting was achieved by tilting the sample. Then either the excess solution was removed with cleanroom paper and the rest left to evaporate in ambient air, or all of the solution was let to evaporate in ambient air. SiO_2/Si substrates with 288 nm thick oxide layer were used in conjunction with copper when graphene growth was not necessary, i.e., when testing temperature stability. Complete wetting of said SiO_2/Si substrates by nanoflake solutions was nigh impossible due to silicon's hydrophobicity, thus a 5 min soft oxygen plasma treatment (see Section 3.4) was used to activate the surface and gain hydrophilicity, after which complete wetting was achieved with a uniform distribution of nanoflakes.

3.2 Mechanical exfoliation of hBN

Mechanical exfoliation of hBN was used to obtain large flakes of hBN on a copper substrate prior to CVD graphene growth. A small piece ($\sim$0.5 mm $\times$ 0.5 mm) of hBN was applied on a piece of dicing tape (Ultron Systems), the tape was then folded over and the flake was pressed hard with fingers following an unfolding of the tape. This cleaves the hBN flake so that some of it is left on a new spot on the dicing tape, thereby thinning the initial flake. The process is repeated over several tens of times in order to get a good, uniform distribution of hBN on the tape over an area of $\sim$1 cm $\times$ 1 cm. Lastly, the tape was firmly pressed with fingers on a clean, electrochemically polished piece of copper foil. Some hBN flakes were transferred from the tape to the copper foil by slowly separating the two.

The electrochemical polishing process consisted of submerging $\sim 2 \times 4$ cm piece of copper foil in a solution of 25 ml of DI-water, 12.5 ml of phosphoric acid, 12.5 ml of ethanol, 2.5 ml of isopropanol and 0.4 g of urea (solution mixture originally from [76]). A second piece of copper foil was used as a counter electrode, where the distance between the electrodes was $\sim$2 cm and polishing time was 60 s with applied voltages of 5 V (producing a current of $\sim$800 mA).

Transfer on a non-polished copper was done by the aforementioned method and by means of viscoelastic stamping. In this process the flakes are transferred from the

exfoliation tape on a viscoelastic material, such as Polydimethylsiloxane (PDMS) by pressing the two together and separating them. Afterward, a micromechanical stage is used to align the stamp with a specific spot on the substrate. The stage is used to press the two together and slowly peel the stamp off of the substrate, thereby transferring individual flakes on a predetermined position. More detailed process is described elsewhere [84].

3.3 Graphene growth process

Graphene growth was done in a vertical, cold-wall CVD apparatus (Aixtron Black Magic 6-inch) on commercial copper foils (with deposited TMD nanoflakes explained in Section 3.1) measuring 25 µm in thickness. Each run started from ambient temperature, reaching 980 °C and 1100 °C for bottom and top heaters respectively with heating rate of ∼90 °C/min. Heating was done under 500 sccm of argon and 1000 sccm of hydrogen gas while keeping the pressure at constant 25 mbar. After reaching the desired temperatures, a short 5 min annealing step was performed. Subsequent growth step was done under 2100 sccm of argon, 18 sccm of hydrogen and 3 sccm of methane, with growth time of 75 s and pressure of 25 mbar. After the growth step, heating was switched off and the furnace was cooled down under 4000 sccm of argon. Samples were removed at temperatures less than 150 °C to prevent oxidation. See Figure 9 for an example.

Transfer of graphene on copper to a SiO_2/Si chip (with 288 nm thick oxide layer) was done with two different methods, both of which involve Polymethyl Methacrylate (PMMA) support layer. The first method was a wet transfer where the top side of copper–graphene structure was covered with PMMA and it was left to cure in ambient air (∼15 min). Then hard oxygen plasma (RIE, see Section 3.4) was applied to the backside graphene for 2 minutes to remove it. This step is crucial as the backside graphene will hinder the etching of copper as well as contaminate the sample after the etching process is done (small graphene flakes will be deposited on the sample). The remaining copper is etched away with 0.1 mol/l Ammonium Persulfate (APS) overnight. The transparent graphene/PMMA structure is picked up with SiO_2/Si chip and put to deionized water (DI-water) to remove excess APS left on the structure. Afterward the structure is picked up again on a SiO_2/Si chip and gently blow-dried with nitrogen. Then the complete structure is baked at 140 °C for 2 minutes on a hotplate to re-flow the PMMA. This step will remove some of the graphene wrinkles, produced by incomplete contact of graphene and SiO_2/Si and by small amounts of water being trapped between graphene and SiO_2/Si substrate [85]. After the baking PMMA is removed with acetone leaving only the graphene on SiO_2/Si. The second method was a bubbling transfer method, where the graphene/PMMA stack is removed from the copper substrate through electrochemical hydrogen evolution at the graphene/copper interface; the hydrogen bubbles will gently peel the PMMA/graphene stack off of the copper substrate. The bubbling transfer is done in 0.1 mol/l Potassium Hydroxide (NaOH) solution, applying voltages of 1.5–2 V with electrode distances in the ∼10 cm range. Other details between the two transfers are the same. See a diagram of the transfer process in Figure 10.

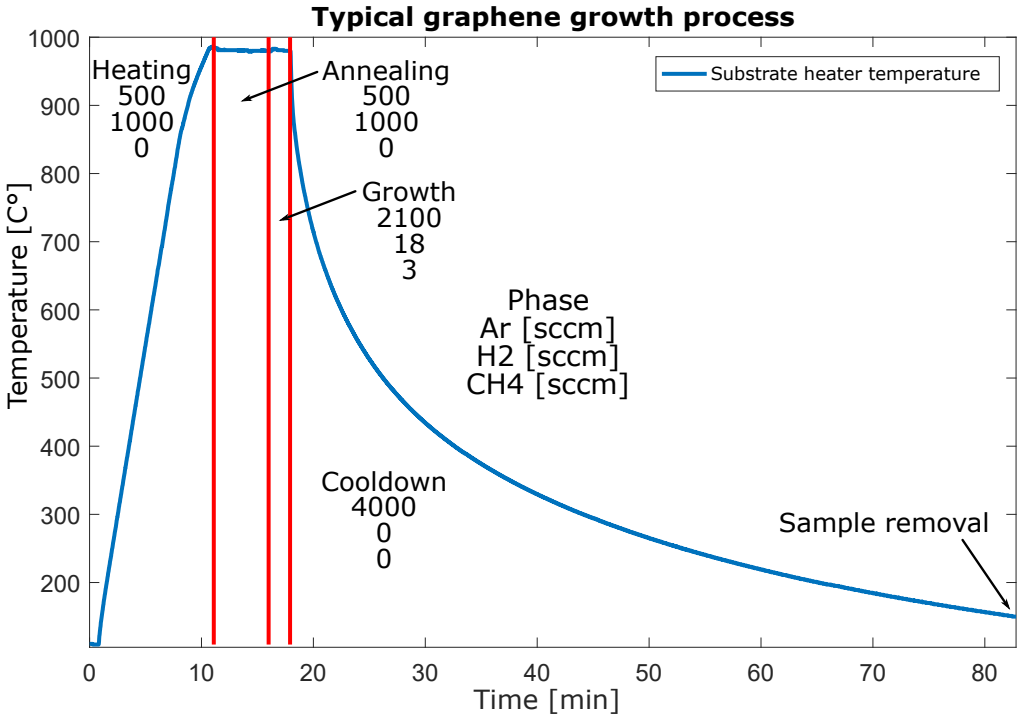

Figure 9: Phases of a typical graphene growth process, numbers under each phase represent the amount of process gases (Ar, H_2 and CH_4, from top to bottom) in standard cubic centimeters. The slope on heating phase is ~90 °C/min and the pressure is a constant 25 mbar during the whole process.

3.4 Plasma etching

Plasma etching can be divided into two different groups, soft and hard plasma etching. Soft plasma etching is an *isotropic* process where usually monatomic species, e.g., oxygen (O_2), hydrogen (H_2) or fluorine (F_2), is used to remove bulks of photoresist or other organic compounds. Generally, terms such as plasma etching and plasma ashing are used for bulk photoresist removal or removal of organic contaminants, while plasma descumming is used for removal of residual photoresist after lithography. Hard plasma etching is an *anisotropic* process in contrast to soft plasma etching. It be further divided into Reactive Ion Etching (RIE) and sputter etching. RIE combines the chemical etching effect of highly reactive ions (and radicals) and physical etching of high-velocity ions impacting the sample. In sputter etching the physical etching is much more prevalent than chemical. Often more complex gases, such as sulfur hexafluoride (SF_6), tetrafluoromethane (CF_4) or fluoroform (CHF_3), are used in hard plasma etching.

Schematic of a conventional parallel plate plasma system (in RIE mode) is shown in Figure 11(b); here the plasma is ionized by applying a strong alternating Electromagnetic (EM) field between two parallel electrodes (a frequency of 13.56 MHz is often used). There are always a few stray electrons in the gas, produced by, e.g., cosmic rays. These stray electrons gain high velocity in the EM field and collide with neutral molecules and break them apart, producing either highly reactive radicals or

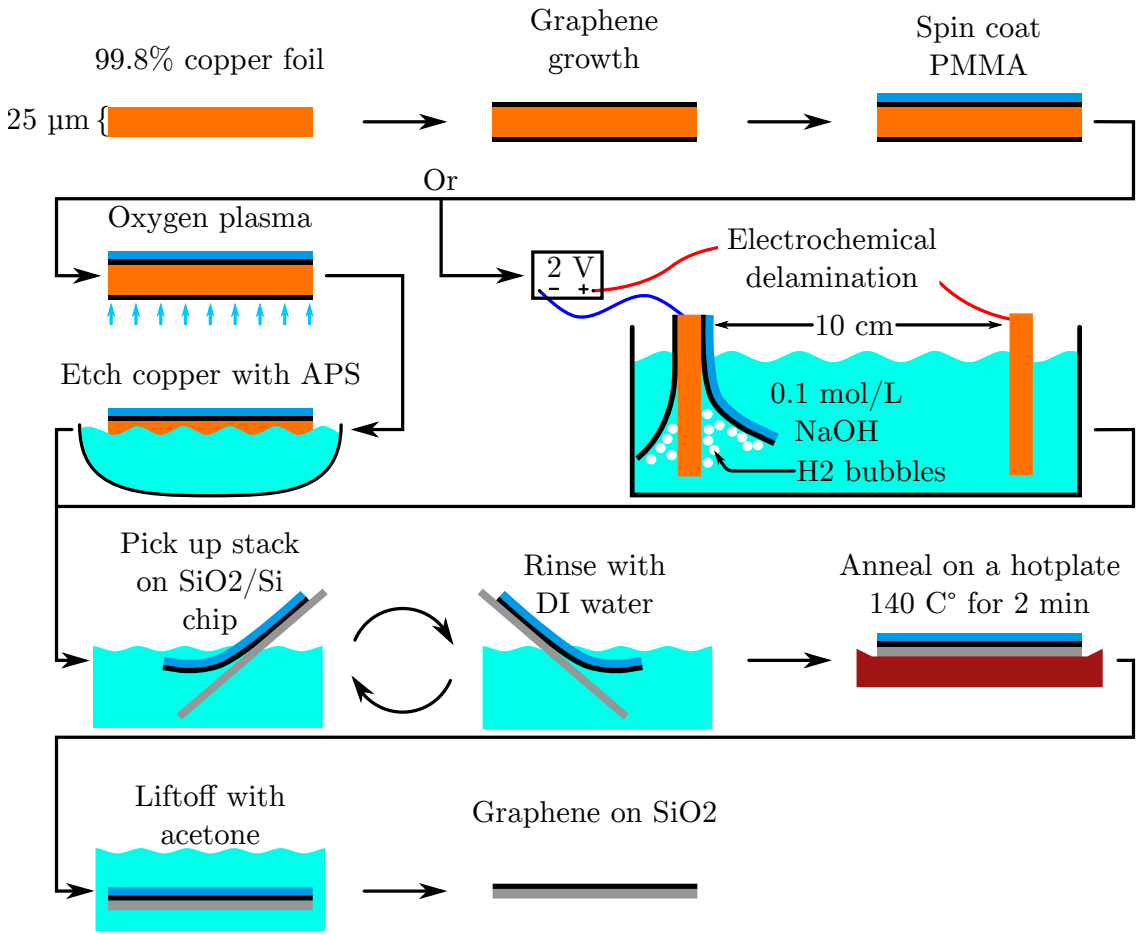

Figure 10: Complete diagram of the transfer process, featuring both transfer methods. Electrochemical delamination method does not require the removal of backside graphene via oxygen plasma, due to it being attracted to the electrochemical cell walls and not being able to contaminate the PMMA/graphene stack.

ions. High enough EM fields will cause an avalanche effect where electrons impacting neutral molecules produce a higher number of electrons than are being lost due to recombination. The effect is also called Townsend discharge. Neither heavy ions nor neutral radicals (and molecules) are affected by the RF field, thus a reactive plasma is formed between the electrodes.

The plasma mode can be changed by setting the substrate on a powered electrode (RIE mode), on ground (plasma etching mode), or on a floating electrode (also plasma etching). In RIE mode, a blocking capacitor is set between the AC generator and the powered electrode; any electrons hitting the powered electrode cannot flow through the capacitor, thus it accumulates charge. The positive ions in the plasma (more specifically, ions in the vicinity of Debye sheath) gain high velocity and directionality towards the negatively charged electrode and the substrate allowing high anisotropy. In plasma etching mode the substrate is set on a grounded or on a floating electrode, thereby removing most charging effects. Thus ion bombardment is very small and chemical etching is prevalent. See Figure 11(a) for a conventional barrel type plasma

etching system. Parallel plate system can also be used in plasma etching as in RIE.

In this work a Oxford Instruments PSR900 plasma etcher was used for soft plasma treatments (cleaning and gaining hydrophilic surface on SiO_2/Si chips). Etching was done with 320 sccm of O_2 and power of 600 W for a maximum of 10 minutes. Oxford Instruments PlasmaLab 80 Plus was used in RIE mode. This was done using 45 sccm of O_2 and 5 sccm of Ar and with power of 50 W for 5 minutes.

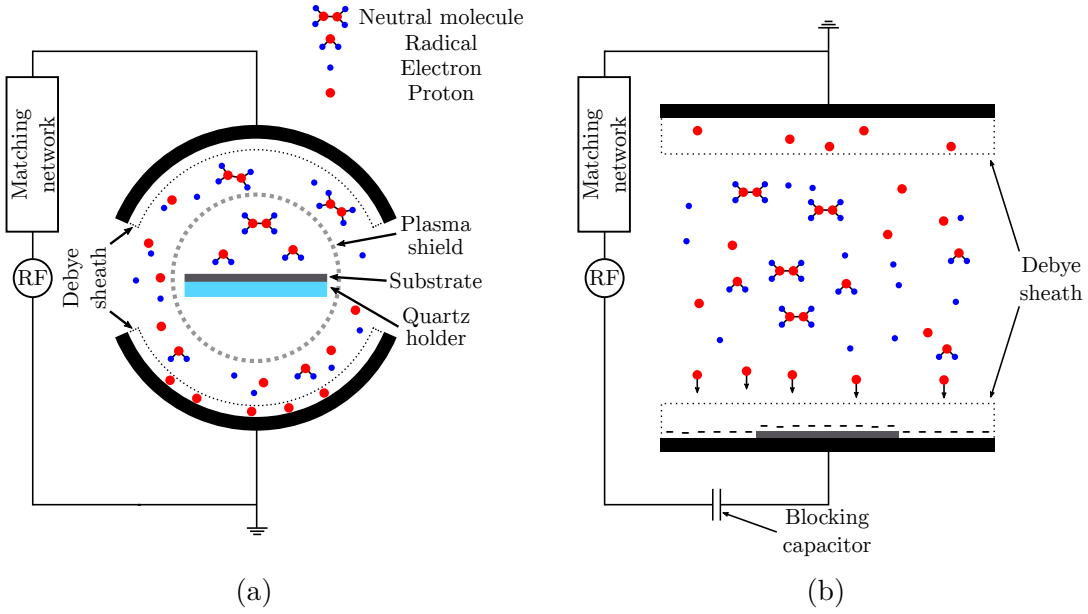

Figure 11: Plasma etching mode in a barrel type reactor (a) and RIE mode in a parallel plate type reactor (b). A Debye sheath forms between the electrodes and the plasma. This sheath is formed due to high mobility electrons flowing into the ground or fed to the external circuit through walls and the electrodes, leading to a higher ion density in the vicinity of them. In RIE mode (b) the charged electrode will repel other electrons, thereby forming a Debye sheath as well. In plasma ashing mode (a) there is only a little charge accumulation on the substrate, thereby allowing mostly chemical etching; this can be enhanced by a plasma shield which only lets through neutral species.

3.5 Scanning electron microscopy

Scanning electron microscopy (SEM) is a very commonly used non-destructive analytical method where electrons (typically accelerated by voltages of 0.1–100 kV) are used to analyze a sample. This is in contrast to, e.g., Raman spectroscopy (see Section 3.6) and conventional optical microscopy both of which use photons. High-energy electrons have a much smaller wavelength (de Broglie) than photons, in the order of 10^{-12} m and 10^{-7} m, respectively; giving electrons better spatial resolution. The wavelength of SEMs is small enough that the signal is not diffraction limited, in contrast to optical microscopes, but aberrations still limit the resolution. Nevertheless, top-of-the-line aberration corrected SEMs are capable of ångström range resolutions.

As these high-energy electrons interact with the atoms of the sample they produce several different signals which can be used to determine its topology and composition. Topological information is generally gained through secondary electrons which are inelastically scattered electrons from the outermost shell of the target atom. In Transmission Electron Microscopy (TEM) the transmitted incident electrons can be used for topology as well as secondary electrons. Compositional information can be gained through, for example

- characteristic x-rays via Energy-dispersive X-ray spectroscopy (EDX),
- Electron Energy Loss Spectroscopy (EELS, only in TEM mode) and
- Backscattered Electrons (BSE).

See Figure 12 for illustrations of where these signals originate.

Most modern SEMs have at least two different detectors for detecting secondary electrons. The most commonly used detectors are Everhart-Thornley (E-T) detector and an in-lens detector. E-T detector consists of a scintillator inside a biased Faraday cage. Depending on the bias (positive or negative) the secondary electrons or BSEs can be collected. The E-T detector is seldom used for BSEs because it collects all the low-energy secondary electrons (including sources that might not be wanted such as electrons generated by high energy BSEs further away in the sample or from the SEM chamber walls). The second type of detector, an in-lens detector, is positioned very close to the sample inside the electron gun column. It is rotationally symmetric along the optical axis. Only the low energy secondary electrons from the very surface of the sample (high surface sensitivity) reach this detector giving it superior topological accuracy.

In this work a Field Emission Zeiss Supra 35 SEM was used with electron energies of 3–5 keV. Low energies are used to prevent damaging graphene.

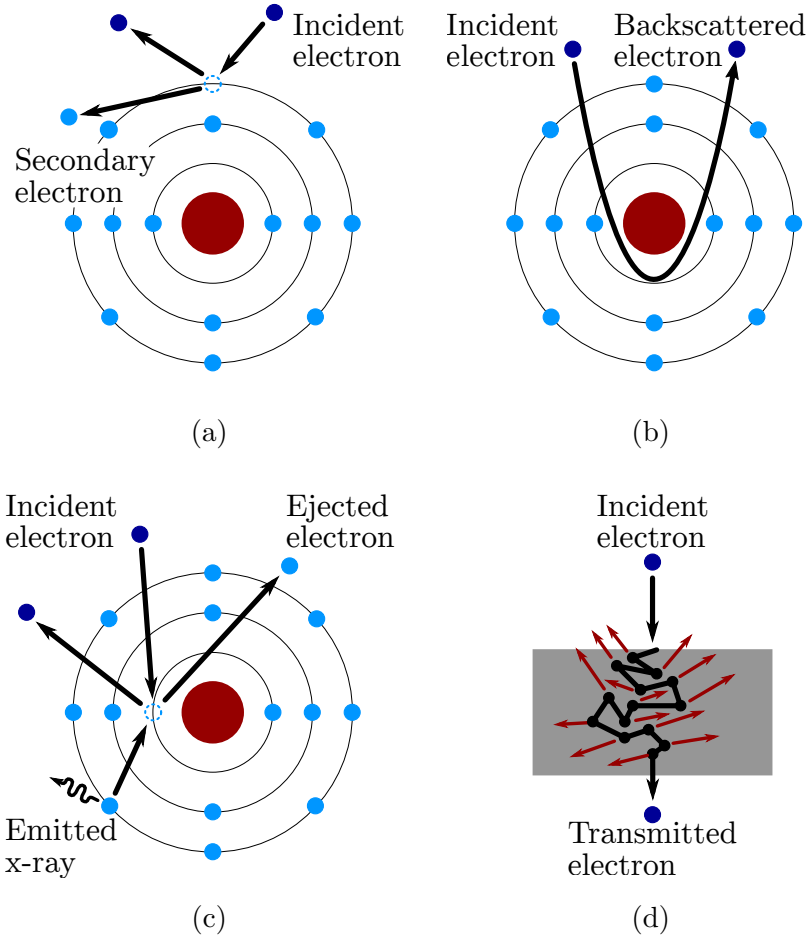

Figure 12: (a) High energy incident electron knocks off loosely bound outer electron (inelastic collision), producing a secondary electron (∼50 eV). (b) The trajectory of incident electron changes due to an elastic collision between it and an atom, producing a high-energy backscattered electron. The cross-section of this depends on the mass of the atom, thus backscattered electrons give information on the mass of the target atom. Elastic collision means no energy loss, therefore BSEs are capable of producing additional secondary electrons. (c) Here the incident electron knocks off one of the more tightly bound electrons (from K-shell), which is then replaced by an electron from the outer shells, thereby emitting an x-ray that is characteristic for the atom, giving elemental information. (d) In transmission mode the incident electron beam goes through the sample, interacting with the atoms in the sample. The incident electrons lose energy due to inelastic collisions, and this loss can be quantified and used to gain information about the composition of the sample. Red arrows denote signals originating from inelastic collisions.

3.6 Raman spectroscopy

Raman spectroscopy is a non-destructive analysis technique for detecting active vibrational and rotational molecular modes (phonons). It is based on Stokes and anti-Stokes Raman scattering of monochromatic light. Raman scattering is the *inelastic* scattering process of photons interacting with matter (in contrast to elastic Rayleigh scattering or to fluorescence). See Figure 13 for more detailed description. An excited phonon is said to be Raman active if it changes the polarizability of a molecule. This is in contrast to infrared spectroscopy, where only the phonons that change the dipole moment of a molecule are infrared active; hence, Raman spectroscopy is a complementary technique to that of infrared spectroscopy.

A very small portion of incident photons are scattered through Raman scattering process, and majority through Rayleigh scattering. The overwhelming effect of this elastic scattering can be removed via, for example, a notch filter. This technique can be used to determine what molecules a material is composed of, as well as give information about, e.g., defects [86], thermal properties [10], crystallinity [87] and doping [88].

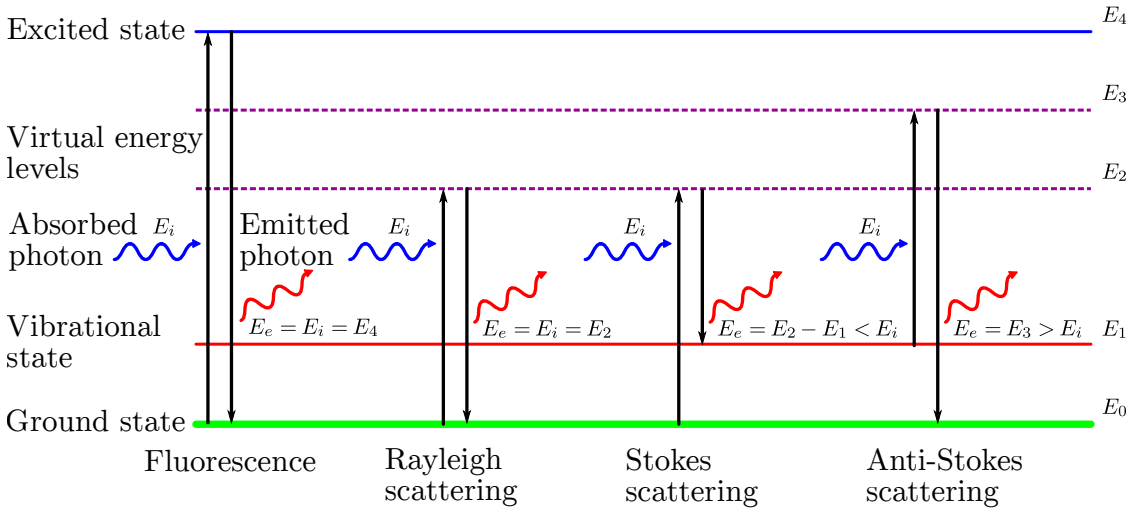

Figure 13: Energy level diagrams of scattering mechanisms (Rayleigh, Stokes, and anti-Stokes) and total absorption (fluorescence) of monochromatic light. In fluorescence the incident photon energy E_i is high enough to transfer the molecule to an excited state. After a resonance lifetime the molecule relaxes and emits a photon with the same energy as the incident photon ($E_e = E_i$). In scattering the incident photon does not have enough energy to transfer the molecule to an excited state. Instead the molecule transfers to a virtual energy state from which it quickly relaxes to a real state. In most cases the molecule relaxes back to the original state and emits a photon with the same energy as the incident photon ($E_e = E_i$); this is known as Rayleigh scattering. In Stokes scattering the molecule relaxes to a higher energy state causing the emitted photon having *less* energy than the incident photon ($E_e < E_i$). In anti-Stokes scattering the molecule is already at a higher energy state as it absorbs a photon. Tt is then transferred to even higher virtual energy state from which it relaxes back to the *ground* state; meaning that the emitted photon has higher energy than the incident photon ($E_e > E_i$).

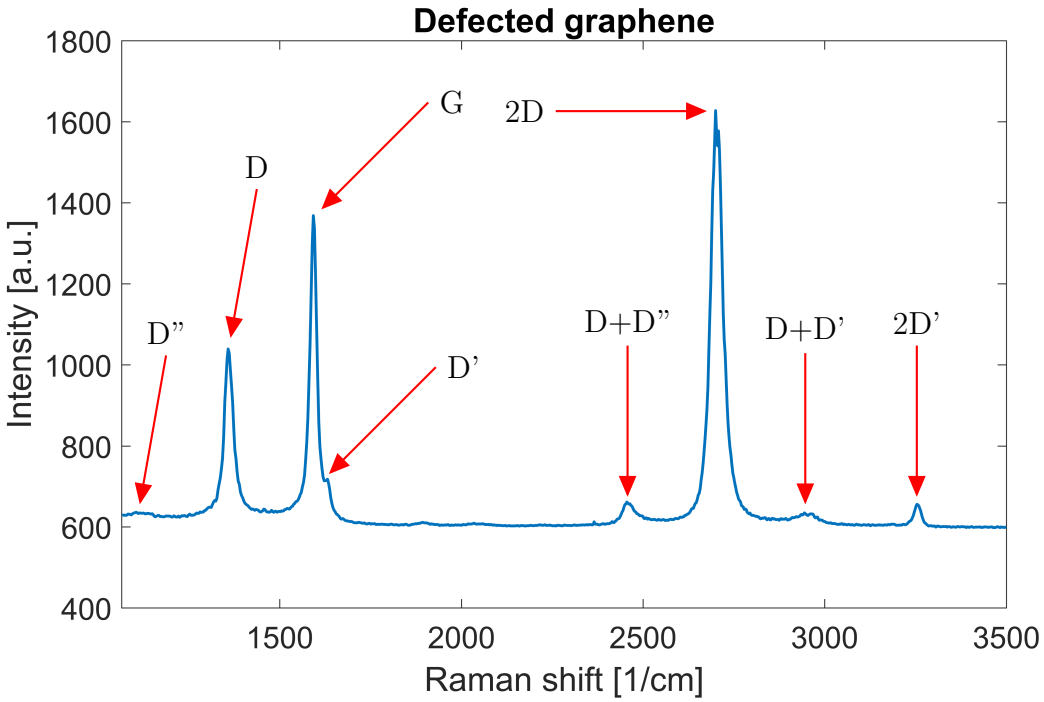

Figure 14: Raman spectrum of defected graphene. Positions for each peak are approximately: 1100 cm^{-1} (D”), 1365 cm^{-1} (D), 1595 cm^{-1} (G), 1635 cm^{-1} (D’), 2458 cm^{-1} (D+D”), 2705 cm^{-1} (2D), 2954 cm^{-1} (D+D’) and 3255 cm^{-1} (2D’).

Graphene is an ideal material for Raman spectroscopy due to lack of a band gap. This makes all wavelength photons resonant thereby allowing Raman spectroscopy to probe the structural and electronic properties of graphene. Graphene has multiple Raman active modes residing in the 1000–3500 cm^{-1} range and one low-frequency mode (C-peak) at ∼42 cm^{-1}. [89] Generally only three modes are used in analysis:

- **D-peak:** The disorder peak originates from the breathing mode of a six-atom base. This mode is activated only when a defect is present. [90]
- **G-peak:** From the high-frequency E^1_{2g} phonon. Always Raman active.
- **2D-peak:** Overtone of the D-peak. Always Raman active due to momentum being conserved through a two-phonon process [91].

Other peaks include the defect induced D’-peak and D”-peak and their overtones. See Figure 14 for an example Raman spectra of defected graphene.

In this work a WITec Alpha 300 RA Raman spectroscope has been used for Raman spectroscopy with a random area of 2500 μm^2 for the measurements. Each measurement was done through a 100x (NA 0.95) objective lens and with a grating of 600 lines/mm. A blue laser having 488 nm excitation wavelength and excitation power of 5 mW was used to obtain the signal. Green laser (513 nm excitation wavelength and same excitation power) was used for verification. Electron Multiplying Charge-Coupling Device (EMCCD) with 0.1 s integration time was used as the operating

mode. Each image is composed of 200 lines per image with 200 points per line, giving resolution of 250 nm per point. These parameters were kept constant throughout the work unless otherwise specified.

The confocally configured WITec Alpha 300 RA Raman spectroscope has (only diffraction limited) lateral resolution of ∼300 nm per pixel and an axial resolution of circa 800 nm.

It is however possible to observe much smaller details than the resolution of the spectroscope would indicate. This is accomplished by using raw oversampling technique [92, 93], with sampling step sizes much lower (e.g., 10 times lower) than the laser spot size. Resolution can be further improved by combining raw oversampling with computational deconvolution. Firstly the geometry of the laser spot, i.e., point spread function (PSF) is extracted from the spectroscope. Then the PSF and the oversampled data is used for computational deconvolution. The deconvolution process tries to extract the real underlying data which is obfuscated by the large laser spot size in comparison to the feature size. The computational oversampling technique is out of scope of this work and raw oversampling was deemed not necessary.

4 Results

4.1 TMD stability and flake distribution

Before any analysis could be done on how graphene grows on TMD nanoflakes, it was necessary to check that the TMDs can withstand the growth environment of graphene in the first place. Several tests were conducted on determining the stability of TMD nanoflakes in this environment. More information of the used TMDs are given in Section 3.1. An analysis of the achieved TMD distributions on copper substrates is also given for a few basic distribution methods.

4.1.1 Thermal stabilities

Initial tests on TMD stability were conducted on standard graphene growth conditions, see Section 3.3. The results are clear: hBN is the only TMD that can withstand the high-temperature growth conditions used in the CVD process. Several tests were made and no Raman signal was found on WS_2 and MoS_2 samples after the process. The following Raman peak positions were found to be useful for identifying the different TMDs: $E^1_{2g}(\Gamma)$ and $A_{1g}(\Gamma)$ modes for WS_2 at ∼353 cm^{-1} and ∼418 cm^{-1}, $E^1_{2g}(\Gamma)$ and $A_{1g}(\Gamma)$ modes for MoS_2 at ∼382 cm^{-1} and ∼404 cm^{-1} and $E^1_{2g}(\Gamma)$ mode for hBN at ∼1371 cm^{-1}. A compiled list of Raman modes for each material can also be found in Table 2. The observed values are close to values found in literature [45, 94, 95]. Small deviations can be explained by possible doping effects due to the solvents where the TMDs are suspended in. Moreover peak positions depend on the thickness of the measured flakes, thus the aforementioned values slightly vary from flake to the next.

Table 2: List of useful Raman modes and their observed approximate positions for identifying WS_2, MoS_2 and hBN.

	Raman mode	
	$E^1_{2g}(\Gamma)$	$A_{1g}(\Gamma)$
WS_2	353 cm^{-1}	418 cm^{-1}
MoS_2	382 cm^{-1}	404 cm^{-1}
hBN	1371 cm^{-1}	-

High temperature (990 °C) and low-temperature (650 °C) annealing for 30 min in pure argon atmosphere were used to test the temperature stability of TMDs. In subsequent experiment hydrogen was introduced into the lower temperature annealing run to see whether hydrogen promotes etching of TMDs (hydrogen promotes the etching of graphene, see Section 2.3.2). Compiled results of different annealing runs for WS_2 and MoS_2 are in Figure 15, experimental data for hBN can be found in the Section 4.2.1. Both WS_2 and MoS_2 have prominent Raman peaks before and after argon and hydrogen annealing runs at 650 °C, therefore it seems that WS_2 and MoS_2 are both stable at low-temperature graphene growth environments.

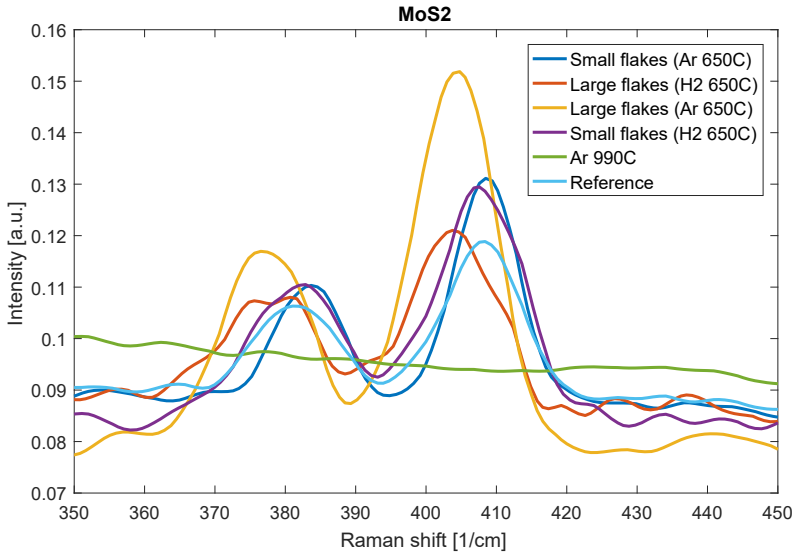

(a)

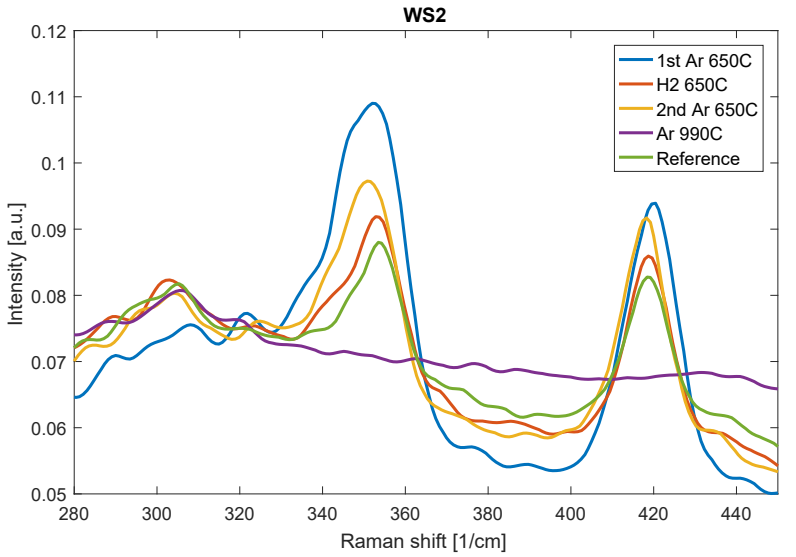

(b)

Figure 15: Effects of low- and high-temperature annealing (650 °C) in argon and hydrogen atmospheres for (a) MoS_2 and for (b) WS_2. It is clear that both materials, MoS_2 and WS_2, can withstand the low-temperature conditions as their respective Raman peaks are clearly visible after the annealing process. Each result is from a different annealing run. The results are compiled from large area scans (2500 µm^2), where only the signals from flakes found in the scan area are averaged over. The second and third (red and yellow) curves of MoS_2 show a larger deviation from the reference result (light blue). This can be explained by those results having fewer ($\sim$10), larger clumps of MoS_2 flakes instead of many (> 40) smaller clumps as in the other results. Clumps are expected because the TMD flake sizes are in the range of a tens to hundreds nanometers, see Section 3.1.

Further study is needed to conclude how graphene grows in presence of these two TMDs. Such low-temperature graphene growth process could possibly be realized by

acetylene-based CVD on nickel substrates [96] or toluene-based on copper substrates [97]. Results for high-temperature annealing are conclusive: neither WS_2 nor MoS_2 can withstand the temperature requirements for high-temperature graphene growth. This can be seen from the non-existent Raman peaks in curves representing 990 °C annealing in Figures 15(a) and 15(b).

Interestingly SEM images before and after low- and high-temperature annealing corroborate with Raman results in the case of WS_2, see Figures 16(a)–(c). Pristine WS_2 nanoflakes present themselves as rectangles or hexagons with clean and sharp corners and edges. Low-temperature annealing sometimes presents itself with new visible structures on top of the nanoflakes, see Figure 16(b). High-temperature annealing considerably changes the morphology of these WS_2 nanoflakes, even up to such extent that sometimes they seem to be melted and fused together, see inset of Figure 16(c). It is also possible that the rectangular or hexagonal morphology of pristine flakes is completely broken and flakes themselves are fragmented into several smaller pieces, see Figure 16(c).

In the case of SEM images of MoS_2 nanoflakes it is almost impossible to tell whether they have gone through high-temperature annealing or not, see Figures 16(d)–(f). When several MoS_2 flakes are investigated, some small differences can be found: the flake size is smaller (though it is hard to say whether this is an artifact of the semi-random deposition process) and some of the flakes seem to have been broken apart, but to much less extent than with WS_2. Apart from rare exceptions the melting effect cannot be seen with MoS_2. Though it should be noted that for MoS_2 the flakes are usually singular and the density is much lower. With WS_2 the situation is different as it is easy to find large bundles of laterally connected flakes. The scarcity of these flakes might be the reason for the melting effect being almost non-existent with MoS_2. Still, many of the MoS_2 flakes do not seem to have gone through any kind of morphological changes due to high-temperature annealing. This is in direct contrast to what Raman results in Figure 15(a) indicate, as they show a complete lack of MoS_2 signal after high-temperature annealing.

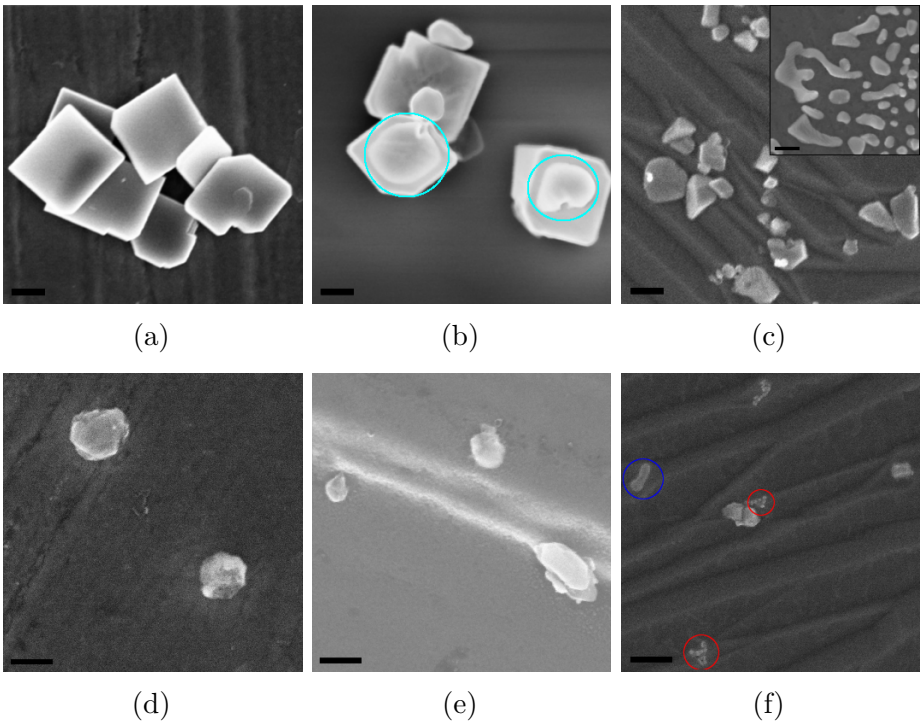

Figure 16: Effects of low- and high-temperature annealing on WS_2 and MoS_2 nanoflakes. Images are ordered by temperature, increasing from left to right (from ambient to 650 °C and finally 990 °C). Top row is for WS_2 and bottom for MoS_2. Due to 650 °C annealing it is sometimes possible to observe new structures on top of WS_2 nanoflakes (cyan circles in (b)). At 990 °C the clean and sharp geometries of pristine WS_2 flakes in (a) break down (c) and even an effect resembling melting can occur (inset of (c)). Pristine MoS_2 nanoflakes of (d) do not seem to have such a clean geometrical morphology as WS_2. On the other hand, MoS_2 nanoflakes do not seem to break down much under annealing. No structural changes seem to happen at a temperature of 650 °C (sub-figure (e)). Sometimes high-temperature annealing at 990 °C breaks MoS_2 nanoflakes and rarely a minute melting effect can be recognized; see red circles and blue circles, respectfully, in (f). Scale bars are 200 nm in each image.

4.1.2 Agglomeration and distribution

Nanoparticles with size in the range of tens to hundreds of nanometers (see Section 3.1 for details) have a very large surface-to-volume ratio; meaning they have a high surface energy. In order for particles to minimize their potential energy small particles tend to aggregate. This can be clearly seen as most of the WS_2 and hBN particles are found in bundles, see Figures 17 and 18. MoS_2 tend to aggregate less, which is probably due to their thickness and lateral size being generally larger.

The bundle size is dependent on the casting method, spin casting can eliminate most of the larger bundles (larger than ∼1 µm lateral size) while sacrificing flake density. Nevertheless, most of the WS_2 and hBN nanoflakes are found in bundles, even if the bundles have a smaller size. Drop casting can results in observable “drying spots” on copper if the excess solution is not removed. This is most evident in areas

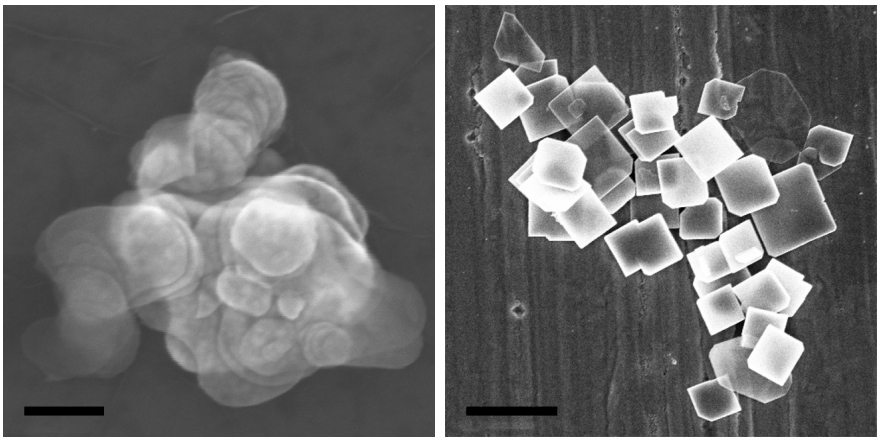

(a) (b)

Figure 17: (a) Bundle of tightly packed hBN nanoflakes. (b) A large bundle of loosely packed WS_2 nanoflakes. Scale bars are 200 nm and 1 µm for (a) and (b), respectively.

where the density of large nanoflake bundles is considerably larger than on the rest of the sample. Even if the excess solution is removed with, e.g., cleanroom paper, the density of large nanoflake bundles is still much higher, see Figure 18 below.

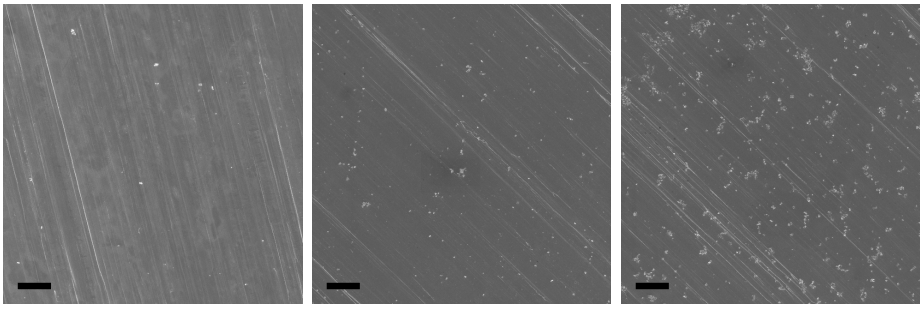

(a) (b) (c)

Figure 18: Examples of density of hBN nanoparticles when using different casting methods. (a) Spin casting (2000 1/min for 30 s), (b) drop casting where the excess solution has been removed with cleanroom paper and (c) drying spot of drop casting method. Scale bars are 10 µm in each image.

Due to the observations on aggregation it is safe to say that the nanoparticles seen with Raman spectroscope are in fact agglomerations of multiple smaller nanoflakes. This was expected even prior to SEM images, due to the fact that the flakes from the Raman spectrographs are larger than expected according to the distributor specifications.

4.2 Graphene growth on hBN

Graphene growth in the presence of hBN nanoflakes is analyzed in this section (neither MoS_2 nor WS_2 can withstand the growth process temperatures). See Section 4.1.1 for further details on the temperature stabilities of MoS_2 and WS_2.

4.2.1 hBN nanoflakes

SEM images after CVD graphene growth indicate that graphene generally grows uniformly around small hBN nanoflakes. Even though the growth seems uniform it is observed that often multiple graphene tears are formed around the nanoflake. This might indicate internal stresses of graphene due to the nanoflake. Contaminant particles on the growth substrate can act as nucleation sites for graphene; however, no such behavior is recognized with small hBN nanoparticles nor do they act as a nucleation sites for multilayer growth. Thus it can be argued that they cannot act as nucleation sites for single layer growth either. Large contaminant particles can also prohibit graphene growth around them, creating voids. This is also the case with large agglomerations of hBN nanoflakes – no graphene grows around them. See Figure 19 for example SEM images of these instances.

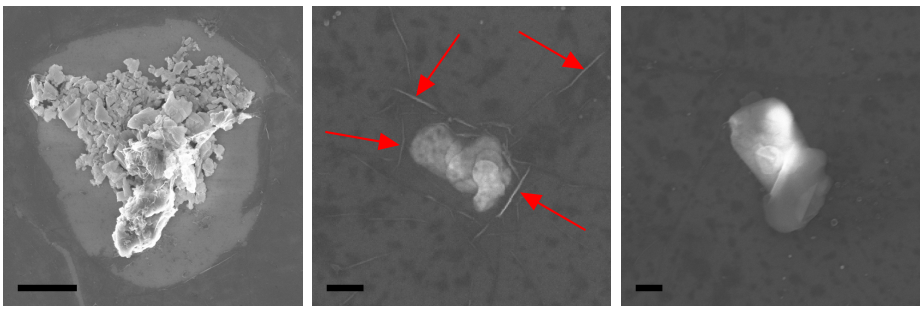

(a) (b) (c)

Figure 19: SEM images of hBN flakes after CVD graphene growth. (a) A large agglomeration of hBN nanoflakes. It can clearly be seen that in this instance a graphene void is produced around the agglomerate. (b) Graphene growing uniformly around a small hBN nanoflake. Some graphene tears have appeared (red arrows), possibly indicating internal stresses of graphene due to the nanoflake. (c) A similar hBN nanoflake with no visible graphene tears. Scale bars are 2 µm for (a) and 200 nm for (b) and (c).

Raman scans on hBN nanoflakes (or bundles of individual flakes as stated in Section 4.1.2) show a clear graphene Raman fingerprint (with no observed increase of defect density around the flakes). However, this does not imply that graphene grows on the surface of the scanned flakes; this is due to the large lateral and axial resolution of Raman (see Section 3.6). A large axial resolution in comparison to the flake thickness can only suggest that graphene grows on the surface or under the flakes, it cannot be asserted which case is true. Moreover, because of large lateral resolution, neither can it be asserted that the observed Raman signal does not originate from possible gaps between singular nanoflakes (as the flakes that the Raman can see are actually agglomerates of individual flakes). The graphene Raman signal can even originate from outside of the observed flakes due to Gaussian point-spread-function of the laser spot and a large spot size.

In order to remove the possible contributions of Raman signal from gaps, outside or the surface of the flakes, hard oxygen plasma (RIE, see Section 3.4) was used to etch away all exposed graphene; notice that graphene under hBN flakes is shielded

from the plasma. Results can be seen in Figure 20, where one can observe that almost all graphene contribution to the Raman signal is gone after RIE treatment. A minute G-peak is still visible and by performing a long integration (5 sec), high-power (15 mW) single point scan it is possible to see the graphene 2D peak. However, due to the minuscule 2D and G peaks it is far more likely that the contribution is merely due to a small amount of graphene that has not completely been etched away but only damaged by RIE, thereby still providing small 2D and G peaks. Furthermore, these small signals cannot be detected on every observed hBN flake, only on some of them.

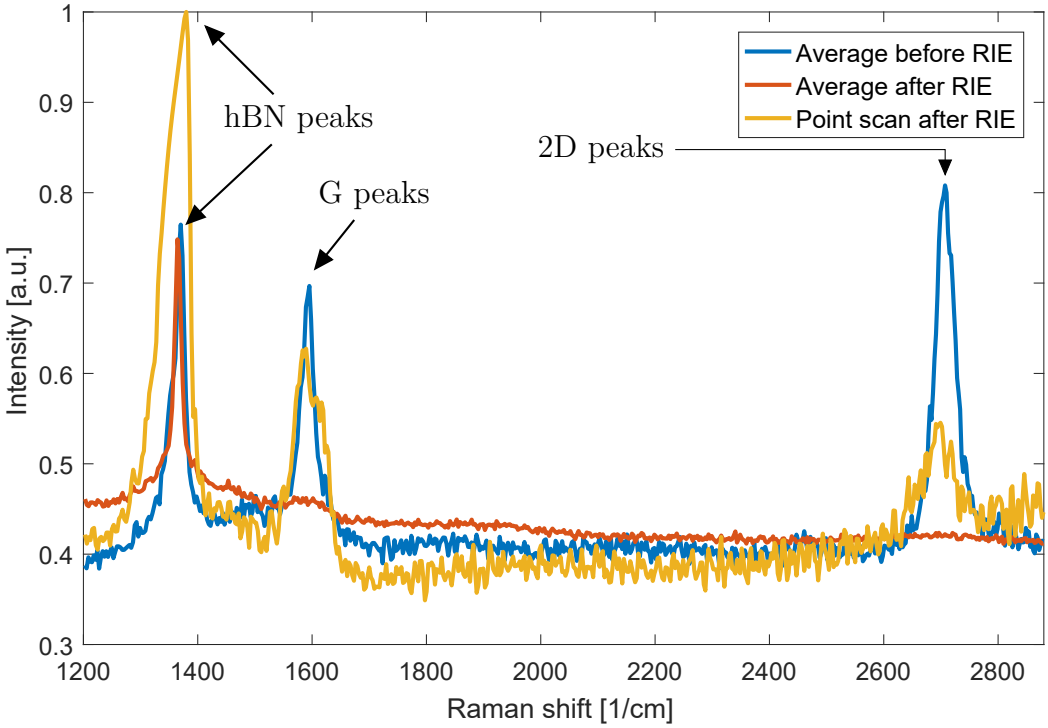

Figure 20: Raman spectroscopy results of hBN nanoflakes on copper after graphene growth (background signal of copper has been computationally removed). The blue line shows results of a single 50×50 µm Raman scan where the spectrum has been averaged over only the hBN flake positions. The graphene fingerprint of peaks 2D and G ($\sim$2707 cm^{-1} and $\sim$1593 cm^{-1}, respectively) are clearly visible; hBN peak can be seen at $\sim$1371 cm^{-1}. Results after RIE treatment are seen in red ($\sim 15 \times 19$ µm area, different position), graphene peaks are almost completely gone (small peak at G-peak position can be seen). A single point scan with long integration time (5 sec) and high laser power (15 mW) is shown in yellow. A very faint 2D and G peaks can be observed, probably due to some remaining graphene after the RIE treatment.

These results are also corroborated by *failed* graphene transfer processes (see Section 3.3 for transfer process details). In a failed scenario graphene can be accidentally removed from the SiO_2/Si substrate surface at the polymer removal step due to a lack of adhesion between SiO_2 and graphene. In this case it is still possible for hBN flakes to be adhered on the SiO_2 surface, effectively detaching the nanoflakes

from the graphene layer. Subsequent Raman scans show no graphene signal from the position of hBN flakes which corroborates that graphene does not grow under hBN nanoflakes.

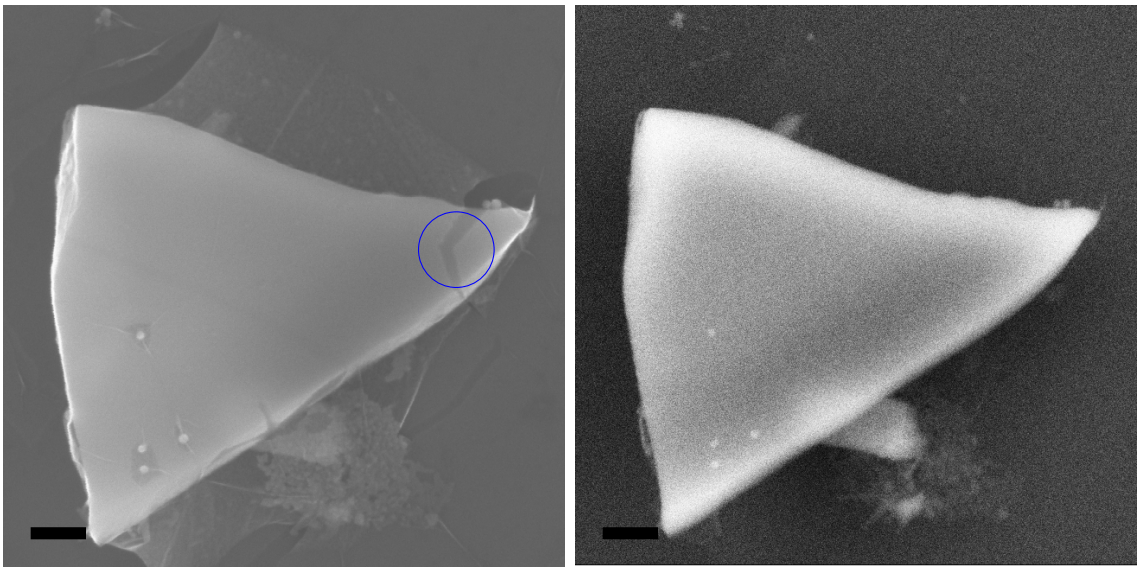

(a)

(b)

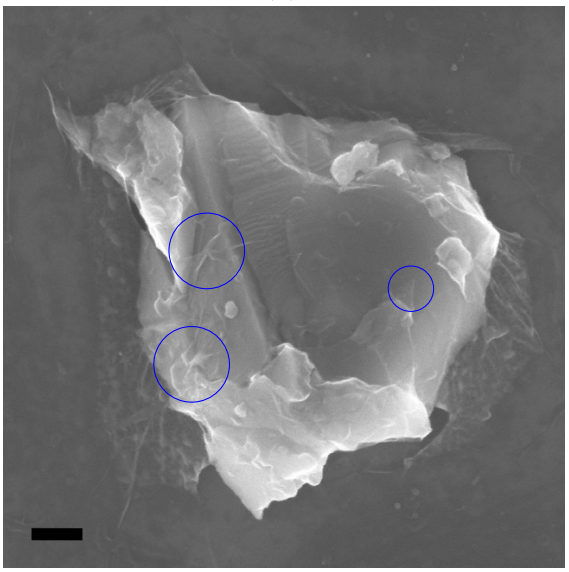

(c)

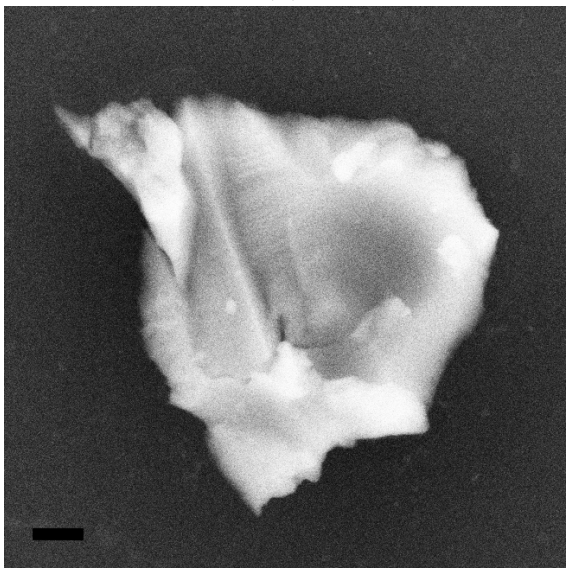

(d)

Figure 21: SEM images of two large hBN nanoflakes, (a) and (c), after transfer to SiO_2/Si substrates, as well as their respective SE2 (E-T detector) SEM images (b) and (d). The blue circles in (d) look like graphene wrinkles on the hBN flake and the blue circle in (a) appears to be a crack in the graphene, indicating almost complete coverage of graphene on the hBN flake. These claims are corroborated by the fact that all of the structures disappear in the SE2 images indicating them being thin and on the surface. Scale bars are 200 nm in each figure.

Graphene appears not to grow below hBN nanoflakes which means that either

is does not grow at all where there is hBN or it grows on the surface. As stated earlier, the resolution of Raman inhibits the study of graphene growth on the surface of nanoflakes. While Raman would ascertain the presence of graphene, SEM can give information on the subject as well. After the transfer process of graphene to SiO_2/Si substrates it is possible to find some large (in comparison to the median size) nanoflakes that appear to have formations resembling graphene growing on top of the flake, see Figure 21

4.2.2 Lorentzian-peak center-position filter

After hBN nanoflake dispersion and subsequent graphene growth, the stack is transferred on a SiO_2/Si substrate to get an atomically flat and insulating surface. This process also increases the signal to noise ratio due to the absence of fluorescence from the copper substrate. This will make it much easier to see graphene and hBN separately when using Raman spectroscopy.

Unfortunately the CVD process used here has not been completely optimized resulting in numerous defect spots on the grown graphene. These spots can be seen in the Raman spectrograph in the disorder band (D-band at 1300–1400 cm^{-1}). The hBN Raman peak resides in the middle of this band (hBN peak is at $\sim$1371 cm^{-1}). This makes it hard to distinguish between small hBN flakes and graphene defect spots unless Lorentzian-peak center-position filtering is used.

It was observed that the general defect spots have less intense Raman signal and much more varied peak center position than hBN. More importantly, the peak center position of D-band varies greatly from pixel to pixel whereas the entire hBN flake resides near the 1371 cm^{-1} position. Thereby hBN can be distinguished from general defect spot by: filtering out too large variations from the 1371 cm^{-1} value, considering only areas where multiple pixels reside near this value and possibly filtering out signals having too small intensity. In its entirety the filtering process is as follows:

1. Take the Lorentzian fit of the target area in the range of circa 1350–1395 cm^{-1}. The range itself is arbitrary as long as the hBN peak resides in the middle of it and is wide enough for filtering.

2. Filter out any peaks with center position less than 1367 cm^{-1} or more than 1374 cm^{-1} (the values can vary 1–3 cm^{-1} between scans and should be manually adjusted).

3. Remove too small areas by utilizing 3x3 pixel median filter.

4. Finally discard areas of too small intensity, if needed.

An example of the filtering process can be seen in Figure 22 where definite hBN flakes can be distinguished in the midst of numerous D-band spots.

Interestingly the D-band spots can hardly be seen at all when the graphene is on copper. Therefore it is much easier to identify hBN flakes by leaving the hBN/graphene stack on copper. The downside of this is that it is almost impossible

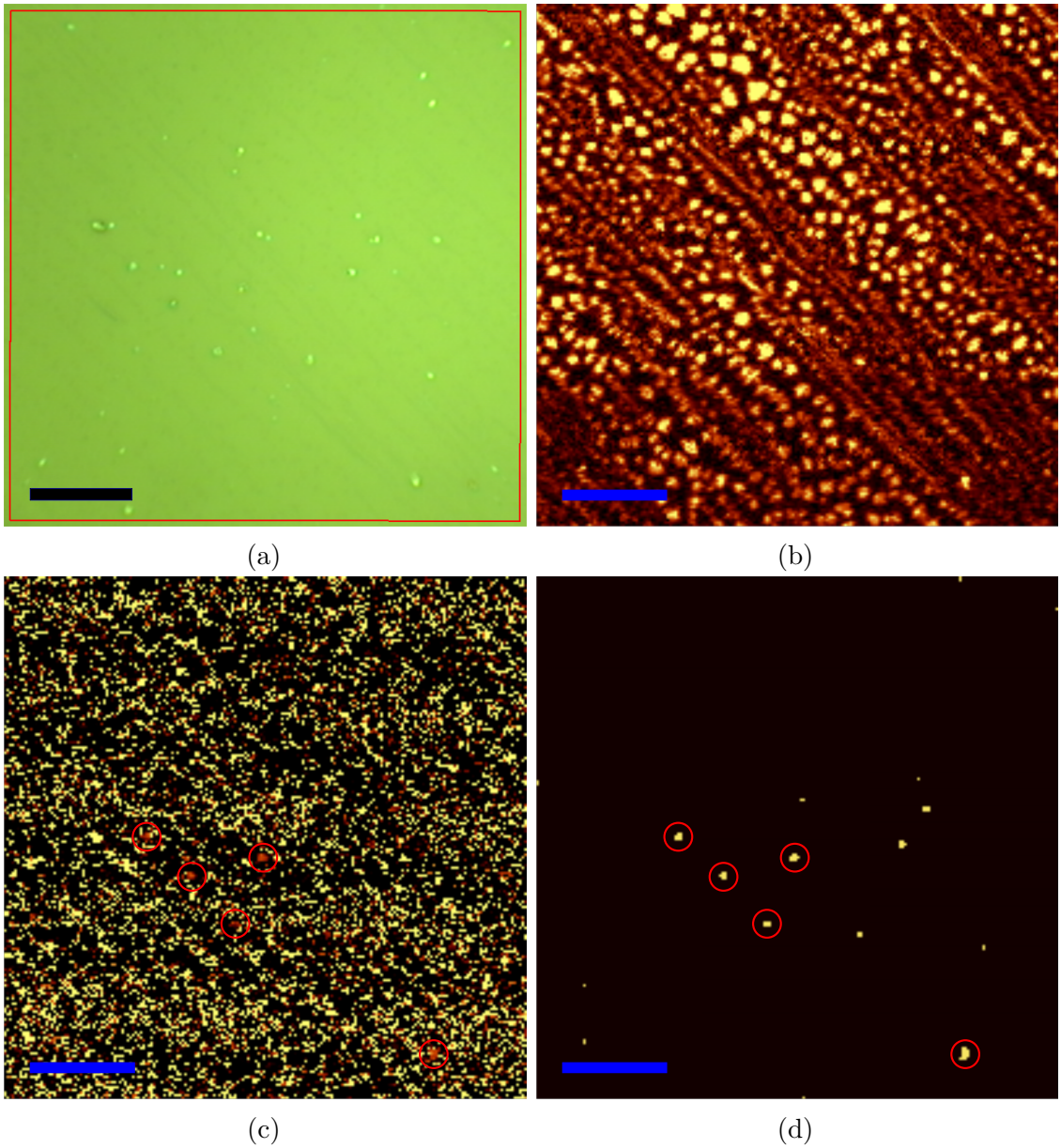

Figure 22: Lorentzian-peak center-position filter –process for hBN. (a) Plain 100x image of the scan area, the red square represents the scanned area. Many flakes can be seen but in order to know whether they are hBN the Raman peak position must be analyzed. (b) D-band (1350–1395 cm^{-1}) Raman map of the scanned area where yellow spots represent high D-band intensity, meaning high disorder. The hBN peak is in the middle of this ($\sim$1371 cm^{-1}), thus the D-band spots completely obscures the hBN signal and it cannot be asserted whether the flakes of (a) are hBN or not. (c) Lorentzian fit center position in the range of 1365–1375 cm^{-1}. A few larger spots that reside between these two values are circled in red, these are hBN agglomerates. Yellow represents values less than 1365 cm^{-1} and larger than 1375 cm^{-1} .(d) Resulting filtered image where hBN flakes have been identified and the same flakes are circled as in (c). Additional hBN flakes have been identified as well. Scale bar in each figure is 10 µm.

to analyze the quality of the CVD graphene on copper due to copper fluorescence. Furthermore, graphene needs to be on an insulating surface for device fabrication. Thus even though hBN is easier to see on copper, the transfer process is still required for device fabrication.

4.2.3 Exfoliated hBN

As determined in Section 4.2.1, using hBN nanoflakes and Raman spectroscopy to find whether graphene can grow on the surface of hBN is unfeasible. This is due to the resolution limitations of confocal Raman spectroscopy. By using larger, mechanically exfoliated hBN flakes, the resolution limitations could be overcome.

A standard exfoliation process with dicing tape was used to produce thin hBN flakes. It was quickly realized that the standard 25 µm thick copper foil used in the CVD process was unusable for mechanical exfoliation. This is due to the lack of adhesion between the flakes and the substrate; no hBN flakes adhered to the substrate after tape removal. Subsequent transfer attempts with a viscoelastic stamping method did not achieve better results. An electrochemical polishing step was included in the transfer process to decrease surface roughness of the copper foil and thereby to increase adhesion between the hBN flakes and the substrate. After the polishing process, a standard mechanical exfoliation using dicing tape was successful in transferring hBN flakes on a copper foil, followed by standard graphene CVD process described in Section 3.3. See Section 3.2 for more information on the exfoliation, the transfer and the electrochemical polishing processes.

SEM revealed that numerous flakes ranging from a few microns to a few tens of microns adhered to the copper surface. By observing the flakes using high magnification it is possible to see various darker formations on the surface, ranging from dark, branch-like structures to a more continuous film, see Figure 23. It seems that small (possibly also thin) flakes tend to produce branch-line formations while the thicker flakes tend to produce continuous, film-like formations. Unfortunately the SEM does not clearly indicate whether there is graphene on the flakes or not. Dark formations indicate higher conductivity but it cannot be ascertained that they are graphene.

Interestingly, the SEM images of mechanically exfoliated flakes differ from those of chemically exfoliated. No aforementioned formations can be observed in the SEM images of chemically exfoliated nanoflakes even though the smaller mechanically exfoliated flakes are laterally smaller than the largest nanoflakes (see Figure 21). Chemically exfoliated flakes also lack the structures present in mechanically exfoliated flakes.

In order to determine whether the formations are graphene or not, Raman spectroscopy was used in the same location as SEM images were taken (positions of Figures 23(c) and 23(d)), see Figure 24. The optical images of the aforementioned flakes show that smaller flakes are much thinner (see Figure 24(b), the optical contrast decreases and the flakes seem more transparent).

However, several thin flakes do not seem to have any graphene on the surface, indicating that the thickness of the flake is not a key factor. One of the thinner flakes

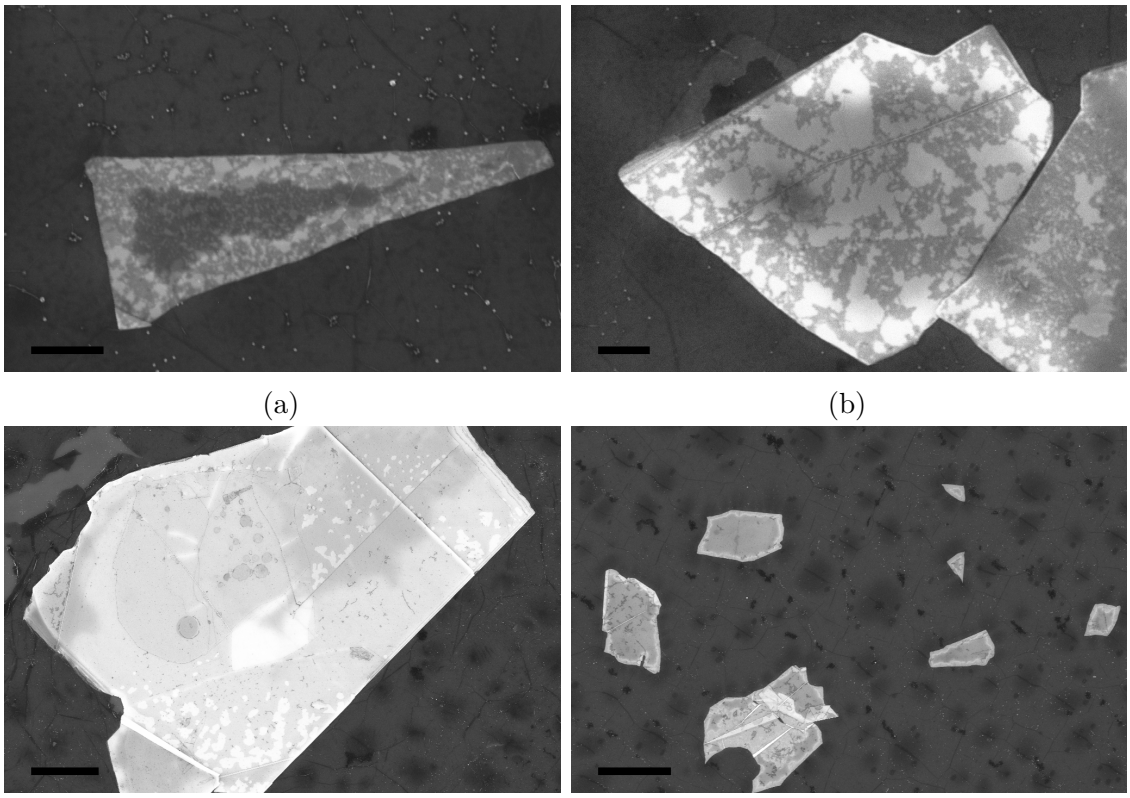

(a) (b)

(c) (d)

Figure 23: (a) A small flake with numerous branch-like structures on the surface and a dark region in the middle. (b) Slightly larger flake with less branch-like structures. (c) A very large flake with no branch-like structures. However, thin darker layer seems to have formed on top of the flake. (d) Numerous flakes with both structures present, several flakes have a darker inner parts, as seen in (a). Scale bars are 500 nm and 4 µm for (a), (b) and (c), (d), respectfully.

does seem to have graphene on the surface, as is confirmed by Raman spectroscopy, but the graphene is not present throughout the entire flake. Even though the Figure 24(a) confirms that the larger flake is bulk, graphene can still grow on it; even if it only grows on a very small portion of the flake, near a defect line. The average Raman scans of both flakes (insets of Figure 24) show that the thin flake has roughly 30 % larger 2D and G peaks, possibly resulting from the difference in thicknesses.

It is not clear why graphene grows on some flakes and not on others. One possibility is that graphene grows much slower on hBN flakes than it does on copper foil due to diminished catalytic pyrolysis. The catalytic properties of copper are hindered by a thick hBN flake, hence the thinner flake would be preferred for graphene growth. This is not easy to determine due to the thickness of both flakes but this effect has been observed with graphene grown on stacked CVD hBN. [59]

Graphene seems to grow only near fault lines and defects (such as seen in optical image of Figure 24 near the graphene) which act as nucleation sites. After nucleation is achieved, graphene can start to grow at a slow rate. Due to graphene growing at

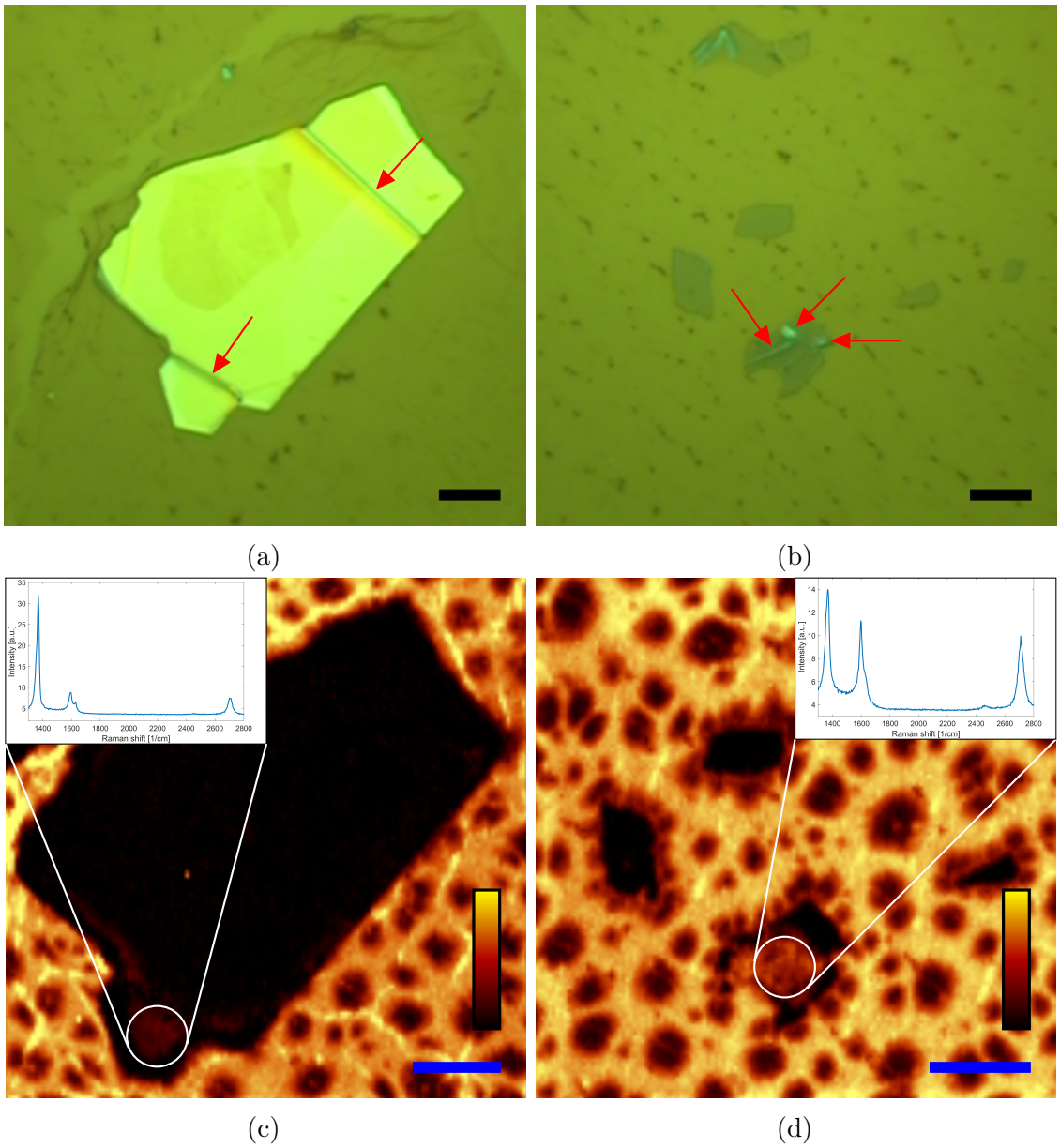

Figure 24: Optical images ((a) and (b)) and graphene 2D peak (2600–2750 cm^{-1}) Raman maps ((c) and (d)) of flakes seen in Figures 23(c) and 23(d), respectfully. (a) Optical images of the large bulk flake and (b) multiple thinner flakes, where a few defects and fault lines are shown with red arrows. (c) Here it can be observed that most of the bulk flake is absent of graphene; however, stronger 2D peak signal does originate from a small part of the flake (white circle) coinciding with one of the defects. Average Raman scan over this area confirms graphene on the surface (inset). (d) Again 2D peak signal originates only one part of a singular flake (white circle). Average Raman scan confirms that graphene is present (inset). Scale bars are 5 µm each and color bars represent a range of 0–50 000 counts on the CCD.

all on the hBN flakes, it can be concluded that hBN has catalytic transparency; even though copper is not exposed, its catalytic properties permeate through the hBN

flakes and graphene is able to grow.

The Raman D-band of Figures 23(c) and 23(d) is shown in Figure 25. One can observe that the outer rim of the hBN flakes have a larger concentration of D-band spots, indicating that hBN flakes diminish the quality of the surrounding graphene. This is in direct contrast to the result seen in the case of hBN nanoflakes, see Section 4.2.1.

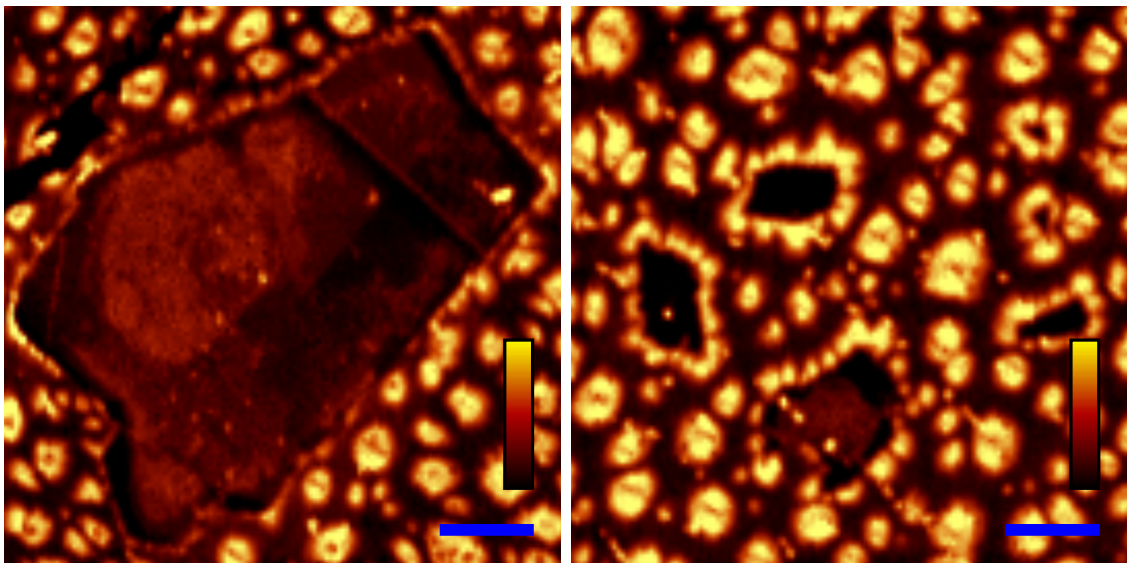

(a) (b)

Figure 25: Effects of the hBN flakes on the graphene measured by Raman D-band (1300–1400 cm^{-1}). One can see the increased density of D-band spots around the hBN flakes in both figures but they are much more prevalent around smaller flakes in figure (b). The scale bars are 5 µm and the color bars represent a range of 6500–70 000 counts on the CCD.

5 Summary and discussion

Graphene is a two-dimensional allotrope of carbon consisting of a hexagonal lattice of sp^2-hybridized atoms. Each carbon atom has three in-plane σ-bonds and one out-of-plane π-bond. Mechanical properties arise from the strong σ-bonds while electrical properties are due to the half filled π-band. formed from overlapping π-bonds. One of graphene's key properties is its flexibility which results from its two-dimensional nature. Graphene's flexibility combined with its electrical properties enables manufacturing of transparent and flexible electronics.

High-quality graphene flakes can be obtained via mechanical exfoliation due to its weak out-of-plane Van der Waals bonding. The method consists of cleaving thin graphite layers from a larger bulk structure with a sticky tape. By thinning this down and pressing it against a substrate, it is possible to transfer one-atom thick graphene layers from the tape to the substrate. Chemical Vapor Deposition (CVD) is the most promising method for large-scale and high-throughput production. In this method graphene is grown at high temperatures on catalytic substrates, such as copper or platinum, by self-limiting catalytic pyrolysis of hydrocarbon precursors.

Transition Metal Dichalcogenides (TMDs) are layered materials consisting of a transition metal (M) and a dichalcogenide (X), described by a generalized chemical formula of MX_2. Like graphene, these compounds are two-dimensional but they also have complementary properties to those of graphene. For instance, some of them have a band gap and/or may be chemically active. These materials can also be manufactured by means of mechanical exfoliation due to their strong in-plane bonds and weak out-of-plane Van der Waals bonds. Some TMDs, such as hexagonal Boron Nitride (hBN), Molybdenum Disulfide (MoS_2) and Tungsten Disulfide (WS_2) can also be manufactured more efficiently using CVD.

TMD-graphene heterostructures are important for exploiting the properties of both materials in a single structure. Cumbersome mechanical exfoliation and manual aligning of cleaved flakes is a slow process, requiring considerable amounts of manual labor and having a very low-throughput. Directly growing CVD graphene on mechanically or chemically exfoliated TMD flakes would facilitate the production of many heterostructures in larger scale with less manual labor.

Due to having three distinctive Raman peaks graphene is usually analyzed with confocal Raman spectroscopy which is a fast and reliable method. Graphene's three Raman peaks makes it possible to analyze, e.g., layer count, doping, defects, general quality, stacking order and stress. Other methods, such as Scanning Electron Microscopy (SEM) and Atomic Force Microscopy (AFM) can be used to obtain complementary information. TMDs also have very prominent Raman peaks.

The experiments on the thermal stability of TMDs (hBN, MoS_2 and WS_2) indicated that only hBN is stable enough to be used in a standard methane based CVD graphene growth process. WS_2 and MoS_2 break down at the temperatures needed for catalytic pyrolysis of methane. However, the temperature of the CVD process can be decreased by changing the hydrocarbon source from methane to, e.g., acetylene or toluene.

Confocal Raman spectroscopy of heterostructures consisting of chemically exfolia-

ted hBN and CVD graphene was considered almost impossible due to high-resolution requirements. In essence, the Raman laser spot size is too large for analyzing nanoscale flakes with adequate accuracy. This translates into issues such as not being able to remove the Raman signal contribution from outside of flakes, rendering it impossible to confirm whether graphene grows on the surface of hBN nanoflakes. However, the lateral resolution of Raman spectroscopy could be increased by computational oversampling by measuring the geometry of the laser spot and applying deconvolution, possibly making it feasible to be used on analyzing nanoflakes. Another possibility would be to use high resolution Tip Enhanced Raman Spectroscopy (TERS) instead of confocal Raman spectroscopy.

Even though the resolution of confocal Raman spectroscopy was not sufficient to determine whether graphene grows on top of the hBN nanoflakes, it can be used to analyze graphene growth under the flakes via precipitation or intercalation mechanisms. Should this happen, the CVD graphene is shielded from anisotropic etching by the overlying hBN flake. By applying RIE and etching all exposed graphene it was concluded that the graphene does not grow under the hBN nanoflakes.

It was necessary to develop a filtering technique to find small hBN nanoflakes in the midst of highly defective graphene. The reason for this is graphene's Raman disorder peak (D-peak) being in the same position as the hBN Raman peak. Lorentzian-peak center-position filter is a technique which exploits the precise position of Raman hBN peak in relation to the Raman D-peak, the center of which varies along the D-band between 1300 cm^{-1} and 1400 cm^{-1}. By shifting the focus from the entire D-band to a much narrower band of 1367–1374 cm^{-1} and combining this with a median filter, it was possible to differentiate between the hBN and D-band spots (areas of high defect density).

The low-resolution of confocal Raman spectroscopy was overcome by using mechanically exfoliated hBN flakes. This made it possible to analyze micrometer scale flakes instead of chemically exfoliated flakes having sizes in the order of nanometers. Mechanical exfoliation (directly or by PDMS stamping) on untreated, commercially available 25 µm thick copper foils was not successful. This may be due to the lack of adhesion of the rough copper surface. The issue was solved by polishing the copper foils electrochemically prior to mechanical exfoliation. Subsequent graphene growth process and Raman analysis clearly indicated that graphene can grow on the surface of mechanically exfoliated hBN. The CVD graphene does not cover the entire flake but seems to be focused around defects. These possibly act as nucleation sites triggering the start of graphene growth.

References

[1] A. K. Geim and K. S. Novoselov, "The rise of graphene." *Nature Materials*, vol. 6, pp. 183–191, 2007.

[2] N. D. Mermin, "Crystalline order in two dimensions," *Physical Review*, vol. 176, no. 1, pp. 250–254, 1968.

[3] D. Nelson and L. Peliti, "Fluctuations in membranes with crystalline and hexatic order," *Journal de Physique*, vol. 49, no. 1, pp. 139–139, 1988.

[4] K. S. Novoselov, A. K. Geim, S. V. Morozov, D. Jiang, Y. Zhang, S. V. Dubonos, I. V. Grigorieva, and A. A. Firsov, "Electric field effect in atomically thin carbon films," *Science*, vol. 306, no. 5696, pp. 666–669, 2004.

[5] A. Fasolino, J. H. Los, and M. I. Katsnelson, "Intrinsic ripples in graphene," *Nature Materials*, vol. 6, no. 11, pp. 858–861, 2007.

[6] R. Zan, C. Muryn, U. Bangert, P. Mattocks, P. Wincott, D. Vaughan, X. Li, L. Colombo, R. S. Ruoff, B. Hamilton, and K. S. Novoselov, "Scanning tunnelling microscopy of suspended graphene," *Nanoscale*, vol. 4, no. 10, p. 3065, 2012.

[7] J. C. Meyer, A. K. Geim, M. I. Katsnelson, K. S. Novoselov, T. J. Booth, and S. Roth, "The structure of suspended graphene sheets," *Nature*, vol. 446, no. 1, pp. 60–63, 2007.

[8] P. R. Wallace, "The band theory of graphite," *Physical Review*, vol. 71, no. 9, pp. 622–634, 1947.

[9] K. I. Bolotin, K. J. Sikes, Z. Jiang, M. Klima, G. Fudenberg, J. Hone, P. Kim, and H. L. Stormer, "Ultrahigh electron mobility in suspended graphene," *Solid State Communications*, vol. 146, no. 9-10, pp. 351–355, 2008.

[10] A. A. Balandin, S. Ghosh, W. Bao, I. Calizo, D. Teweldebrhan, F. Miao, and C. N. Lau, "Superior thermal conductivity of single-layer graphene," *Nano Letters*, vol. 8, no. 3, pp. 902–907, 2008.

[11] K. F. Mak, M. Y. Sfeir, Y. Wu, C. H. Lui, J. A. Misewich, and T. F. Heinz, "Measurement of the Optical Conductivity of Graphene," *Physical Review Letters*, vol. 101, no. 19, p. 196405, 2008.

[12] C. Lee, X. Wei, J. W. Kysar, and J. Hone, "Measurement of the Elastic Properties and Intrinsic Strength of Monolayer Graphene," *Science*, vol. 321, no. 18 July 2008, pp. 385–388, 2008.

[13] J. S. Bunch, S. S. Verbridge, J. S. Alden, A. M. Van Der Zande, J. M. Parpia, H. G. Craighead, and P. L. McEuen, "Impermeable atomic membranes from graphene sheets," *Nano Letters*, vol. 8, no. 8, pp. 2458–2462, 2008.

[14] K. S. Novoselov, A. K. Geim, S. V. Morozov, D. Jiang, M. I. Katsnelson, I. V. Grigorieva, S. V. Dubonos, and A. A. Firsov, "Two-dimensional gas of massless Dirac fermions in graphene," *Nature*, vol. 438, no. 7065, pp. 197–200, 2005.

[15] K. S. Novoselov, Z. Jiang, Y. Zhang, S. V. Morozov, H. L. Stormer, U. Zeitler, J. C. Maan, G. S. Boebinger, P. Kim, and A. K. Geim, "Room-Temperature Quantum Hall Effect in Graphene," *Science*, vol. 315, no. 5817, pp. 1379–1379, 2007.

[16] Z. Qiao, S. A. Yang, W. Feng, W.-K. Tse, J. Ding, Y. Yao, J. Wang, and Q. Niu, "Quantum Anomalous Hall Effect in Graphene from Rashba and Exchange Effects," *Physical Review B - Condensed Matter and Materials Physics*, vol. 82, no. 1, p. 161414, 2010.

[17] Y.-M. Lin, C. Dimitrakopoulos, K. A. Jenkins, D. B. Farmer, H.-Y. Chiu, A. Grill, and P. Avouris, "100 GHz Transistors from Wafer Scale Epitaxial Graphene," *Science (New York, N.Y.)*, vol. 327, p. 662, 2010.

[18] L. Liao, Y.-C. Lin, M. Bao, R. Cheng, J. Bai, Y. Liu, Y. Qu, K. L. Wang, Y. Huang, and X. Duan, "High-speed graphene transistors with a self-aligned nanowire gate," *Nature*, vol. 467, no. 7313, pp. 305–8, 2010.

[19] R. Lai, X. B. Mei, W. R. Deal, W. Yoshida, Y. M. Kim, P. H. Liu, J. Lee, J. Uyeda, V. Radisic, M. Lange, T. Gaier, L. Samoska, and A. Fung, "Sub 50 nm InP HEMT device with Fmax greater than 1 THz," *Technical Digest - International Electron Devices Meeting, IEDM*, vol. 3, pp. 609–611, 2007.

[20] X. Mei, W. Yoshida, M. Lange, J. Lee, J. Zhou, P.-H. Liu, K. Leong, A. Zamora, J. Padilla, S. Sarkozy, R. Lai, and W. R. Deal, "First Demonstration of Amplification at 1 THz Using 25-nm InP High Electron Mobility Transistor Process," *IEEE Electron Device Letters*, vol. 36, no. 4, pp. 327–329, 2015.

[21] J. Lee, T. J. Ha, H. Li, K. N. Parrish, M. Holt, A. Dodabalapur, R. S. Ruoff, and D. Akinwande, "25 GHz embedded-gate graphene transistors with high-K dielectrics on extremely flexible plastic sheets," *ACS Nano*, vol. 7, no. 9, pp. 7744–7750, 2013.

[22] N. Petrone, I. Meric, T. Chari, K. L. Shepard, and J. Hone, "Graphene field-effect transistors for radio-frequency flexible electronics," *IEEE Journal of the Electron Devices Society*, vol. 3, no. 1, pp. 44–48, 2015.

[23] H. Zhou, J.-H. Seo, D. M. Paskiewicz, Y. Zhu, G. K. Celler, P. M. Voyles, W. Zhou, M. G. Lagally, and Z. Ma, "Fast flexible electronics with strained silicon nanomembranes." *Scientific Reports*, vol. 3, p. 1291, 2013.

[24] C. Wang, J.-C. Chien, H. Fang, K. Takei, J. Nah, E. Plis, S. Krishna, A. M. Niknejad, and A. Javey, "Self-aligned, extremely high frequency III–V metal-oxide-semiconductor field-effect transistors on rigid and flexible substrates," *Nano Letters*, vol. 12, no. 8, pp. 4140–4145, 2012.

[25] G. Giovannetti, P. A. Khomyakov, G. Brocks, P. J. Kelly, and J. Van Den Brink, "Substrate-induced band gap in graphene on hexagonal boron nitride: Ab initio density functional calculations," *Physical Review B - Condensed Matter and Materials Physics*, vol. 76, no. 7, pp. 2–5, 2007.

[26] J. Xue, J. Sanchez-Yamagishi, D. Bulmash, P. Jacquod, A. Deshpande, K. Watanabe, T. Taniguchi, P. Jarillo-Herrero, and B. J. LeRoy, "Scanning tunnelling microscopy and spectroscopy of ultra-flat graphene on hexagonal boron nitride." *Nat. Mater.*, vol. 10, no. 4, pp. 282–285, 2011.

[27] M. Y. Han, B. Özyilmaz, Y. Zhang, and P. Kim, "Energy band-gap engineering of graphene nanoribbons," *Physical Review Letters*, vol. 98, no. 20, pp. 1–4, 2007.

[28] Y. Zhang, T.-T. Tang, C. Girit, Z. Hao, M. C. Martin, A. Zettl, M. F. Crommie, Y. R. Shen, and F. Wang, "Direct observation of a widely tunable bandgap in bilayer graphene." *Nature*, vol. 459, no. 7248, pp. 820–3, 2009.

[29] W. Bludau, A. Onton, and W. Heinke, "Temperature dependence of the band gap of silicon," *Journal of Applied Physics*, vol. 45, no. 4, pp. 1846–1848, 1974.

[30] K. V. Emtsev, A. Bostwick, K. Horn, J. Jobst, G. L. Kellogg, L. Ley, J. L. McChesney, T. Ohta, S. A. Reshanov, J. Röhrl, E. Rotenberg, A. K. Schmid, D. Waldmann, H. B. Weber, and T. Seyller, "Towards wafer-size graphene layers by atmospheric pressure graphitization of silicon carbide." *Nature Materials*, vol. 8, no. 3, pp. 203–207, 2009.

[31] C. Berger, X. Wu, N. Brown, C. Naud, X. Li, Z. Song, D. Mayou, T. Li, J. Hass, A. Marchenkov, E. H. Conrad, P. N. First, and W. A. De Heer, "Electronic Confinement and Coherence in Patterned Epitaxial Graphene," *Science*, vol. 312, no. May, pp. 1191–1196, 2006.

[32] V. Ramachandran, M. F. Brady, A. R. Smith, R. M. Feenstra, and D. W. Greve, "Preparation of atomically flat surfaces on silicon carbide using hydrogen etching," *Journal of Electronic Materials*, vol. 27, no. 4, pp. 308–312, 1998.

[33] Y. Hernandez, V. Nicolosi, M. Lotya, F. Blighe, Z. Sun, S. De, I. T. McGovern, B. Holland, M. Byrne, Y. Gunko, J. Boland, P. Niraj, G. Duesberg, S. Krishnamurti, R. Goodhue, J. Hutchison, V. Scardaci, A. C. Ferrari, and J. N. Coleman, "High yield production of graphene by liquid phase exfoliation of graphite," *Nature Nanotechnology*, vol. 3, no. 9, pp. 563–8, 2008.

[34] R. Park, S.; Ruoff, "Chemical methods for the production of graphenes," *Nature Nanotechnology*, vol. 4, no. march, pp. 217–224, 2009.

[35] Q. H. Wang, K. Kalantar-Zadeh, A. Kis, J. N. Coleman, and M. S. Strano, "Electronics and optoelectronics of two-dimensional transition metal dichalcogenides," *Nature Nanotechnology*, vol. 7, no. 11, pp. 699–712, 2012.

[36] T. Kanazawa, T. Amemiya, A. Ishikawa, V. Upadhyaya, K. Tsuruta, T. Tanaka, and Y. Miyamoto, "Few-layer HfS2 transistors," *Scientific Reports*, vol. 6, no. October 2015, p. 22277, 2016.

[37] B. Sipos, A. F. Kusmartseva, A. Akrap, H. Berger, L. Forró, and E. Tutis, "From Mott state to superconductivity in 1T-TaS2." *Nature Materials*, vol. 7, no. 12, pp. 960–5, 2008.

[38] D. Xiao, G. B. Liu, W. Feng, X. Xu, and W. Yao, "Coupled spin and valley physics in monolayers of MoS 2 and other group-VI dichalcogenides," *Physical Review Letters*, vol. 108, no. 19, pp. 1–5, 2012.

[39] R. Gordon, D. Yang, E. Crozier, D. Jiang, and R. Frindt, "Structures of exfoliated single layers of WS2, MoS2, and MoSe2 in aqueous suspension," *Physical Review B*, vol. 65, no. October 2001, pp. 1–9, 2002.

[40] G. Eda, H. Yamaguchi, D. Voiry, T. Fujita, M. Chen, and M. Chhowalla, "Photoluminescence from Chemically Exfoliated MoS2," *Nano Letters*, vol. 12, no. 12, p. 526, 2012.

[41] N. D. Boscher, C. J. Carmalt, and I. P. Parkin, "Atmospheric pressure chemical vapor deposition of wse 2 thin films on glass—highly hydrophobic sticky surfaces," *Journal of Materials Chemistry*, vol. 16, no. 1, pp. 122–127, 2006.

[42] N. D. Boscher, C. J. Carmalt, R. G. Palgrave, J. J. Gil-Tomas, and I. P. Parkin, "Atmospheric pressure CVD of molybdenum diselenide films on glass," *Chemical Vapor Deposition*, vol. 12, no. 11, pp. 692–698, 2006.

[43] K. K. Liu, W. Zhang, Y. H. Lee, Y. C. Lin, M. T. Chang, C. Y. Su, C. S. Chang, H. Li, Y. Shi, H. Zhang, C. S. Lai, and L. J. Li, "Growth of large-area and highly crystalline MoS 2 thin layers on insulating substrates," *Nano Letters*, vol. 12, no. 3, pp. 1538–1544, 2012.

[44] Y. Zhan, Z. Liu, S. Najmaei, P. M. Ajayan, and J. Lou, "Large-area vapor-phase growth and characterization of MoS 2 atomic layers on a SiO 2 substrate," *Small*, vol. 8, no. 7, pp. 966–971, 2012.

[45] Y. H. Lee, X. Q. Zhang, W. Zhang, M. T. Chang, C. T. Lin, K. D. Chang, Y. C. Yu, J. T. W. Wang, C. S. Chang, L. J. Li, and T. W. Lin, "Synthesis of large-area MoS 2 atomic layers with chemical vapor deposition," *Advanced Materials*, vol. 24, no. 17, pp. 2320–2325, 2012.

[46] S. Wu, C. Huang, G. Aivazian, J. S. Ross, D. H. Cobden, and X. Xu, "Vapor–Solid Growth of High Optical Quality MoS 2 Monolayers with Near-Unity Valley Polarization," *ACS Nano*, vol. 7, no. 3, pp. 2768–2772, 2013.

[47] X. Li, W. Cai, J. An, S. Kim, J. Nah, D. Yang, R. Piner, A. Velamakanni, I. Jung, E. Tutuc, S. K. Banerjee, L. Colombo, and R. S. Ruoff, "Large-area

synthesis of high-quality and uniform graphene films on copper foils." *Science (New York, N.Y.)*, vol. 324, no. 5932, pp. 1312–1314, 2009.

[48] P. W. Sutter, J.-I. Flege, and E. A. Sutter, "Epitaxial graphene on ruthenium." *Nature Materials*, vol. 7, no. 5, pp. 406–11, 2008.

[49] Q. Yu, J. Lian, S. Siriponglert, H. Li, Y. P. Chen, and S. S. Pei, "Graphene segregated on Ni surfaces and transferred to insulators," *Applied Physics Letters*, vol. 93, no. 11, pp. 11–14, 2008.

[50] L. Gao, W. Ren, H. Xu, L. Jin, Z. Wang, T. Ma, L.-P. Ma, Z. Zhang, Q. Fu, L.-M. Peng, X. Bao, and H.-M. Cheng, "Repeated growth and bubbling transfer of graphene with millimetre-size single-crystal grains using platinum," *Nature Communications*, vol. 3, p. 699, 2012.

[51] J. Coraux, A. T. N'Diaye, C. Busse, and T. Michely, "Structural coherency of graphene on Ir(111)," *Nano Letters*, vol. 8, no. 2, pp. 565–570, 2008.

[52] S. Y. Kwon, C. V. Ciobanu, V. Petrova, V. B. Shenoy, J. Bareño, V. Gambin, I. Petrov, and S. Kodambaka, "Growth of semiconducting graphene on palladium," *Nano Letters*, vol. 9, no. 12, pp. 3985–3990, 2009.

[53] Z. Sun, Z. Yan, J. Yao, E. Beitler, Y. Zhu, and J. M. Tour, "Growth of graphene from solid carbon sources," *Nature*, vol. 468, no. 7323, pp. 549–552, 2010.

[54] G. Ruan, Z. Sun, Z. Peng, and J. M. Tour, "Growth of Graphene from Food, Insects, and Waste," *ACS Nano*, vol. 5, no. 9, pp. 7601–7607, 2011.

[55] A. Pirkle, J. Chan, A. Venugopal, D. Hinojos, C. W. Magnuson, S. McDonnell, L. Colombo, E. M. Vogel, R. S. Ruoff, and R. M. Wallace, "The effect of chemical residues on the physical and electrical properties of chemical vapor deposited graphene transferred to SiO2," *Applied Physics Letters*, vol. 99, no. 12, pp. 3–5, 2011.

[56] Y. Wang, Y. Zheng, X. Xu, E. Dubuisson, Q. Bao, J. Lu, and K. Ping, "Electrochemical Delamination of CVD Grown Graphene Film : Toward the Recyclable Use of Copper Catalyst," *ACS Nano*, vol. 5, no. 12, pp. 9927–9933, 2011.

[57] C. R. Dean, A. F. Young, I. Meric, C. Lee, L. Wang, S. Sorgenfrei, K. Watanabe, T. Taniguchi, P. Kim, K. L. Shepard, and J. Hone, "Boron nitride substrates for high-quality graphene electronics." *Nature Nanotechnology*, vol. 5, no. 10, pp. 722–726, 2010.

[58] X. Li, C. W. Magnuson, A. Venugopal, J. An, J. W. Suk, B. Han, M. Borysiak, W. Cai, A. Velamakanni, Y. Zhu, L. Fu, E. M. Vogel, E. Voelkl, L. Colombo, and R. S. Ruoff, "Graphene Films with Large Domain Size by a Two-Step Chemical Vapor Deposition Process," *Nano Letters*, vol. 10, no. 11, pp. 4328–4334, 2010.

[59] L. Banszerus, M. Schmitz, S. Engels, J. Dauber, M. Oellers, F. Haupt, K. Watanabe, T. Taniguchi, B. Beschoten, and C. Stampfer, "Ultrahigh-mobility graphene devices from chemical vapor deposition on reusable copper," *Science Advances*, vol. 1, no. 6, pp. e1 500 222–e1 500 222, 2015.

[60] N. Petrone, C. R. Dean, I. Meric, A. M. Van Der Zande, P. Y. Huang, L. Wang, D. Muller, K. L. Shepard, and J. Hone, "Chemical vapor deposition-derived graphene with electrical performance of exfoliated graphene," *Nano Letters*, vol. 12, no. 6, pp. 2751–2756, 2012.

[61] X. Li, C. W. Magnuson, A. Venugopal, R. M. Tromp, J. B. Hannon, E. M. Vogel, L. Colombo, and R. S. Ruoff, "Large-area graphene single crystals grown by low-pressure chemical vapor deposition of methane on copper," *Journal of the American Chemical Society*, vol. 133, no. 9, pp. 2816–2819, 2011.

[62] S. Chen, H. Ji, H. Chou, Q. Li, H. Li, J. W. Suk, R. Piner, L. Liao, W. Cai, and R. S. Ruoff, "Millimeter-Size Single-Crystal Graphene by Suppressing Evaporative Loss of Cu During Low Pressure Chemical Vapor Deposition," *Advanced Materials*, vol. 25, no. 14, pp. 2062–2065, 2013.

[63] H. Tetlow, J. Posthuma de Boer, I. J. Ford, D. D. Vvedensky, J. Coraux, and L. Kantorovich, "Growth of epitaxial graphene: Theory and experiment," *Physics Reports*, vol. 542, no. 3, pp. 195–295, 2014.

[64] M. Batzill, "The surface science of graphene: Metal interfaces, CVD synthesis, nanoribbons, chemical modifications, and defects," *Surface Science Reports*, vol. 67, no. 3-4, pp. 83–115, 2012.

[65] S. Arpiainen, Private communication, Nov. 2016.

[66] C.-T. Au, C.-F. Ng, and M.-S. Liao, "Methane Dissociation and Syngas Formation on Ru, Os, Rh, Ir, Pd, Pt, Cu, Ag, and Au: A Theoretical Study," *Journal of Catalysis*, vol. 185, no. 1, pp. 12–22, 1999.

[67] M. Younessi-Sinaki, E. A. Matida, and F. Hamdullahpur, "Kinetic model of homogeneous thermal decomposition of methane and ethane," *International Journal of Hydrogen Energy*, vol. 34, no. 9, pp. 3710–3716, 2009.

[68] S. Vaidyaraman, W. J. Lackey, P. K. Agrawal, and T. L. Starr, "1-D model for forced flow-thermal gradient chemical vapor infiltration process for carbon/carbon composites," *Carbon*, vol. 34, no. 9, pp. 1123–1133, 1996.

[69] C. Guéret, M. Daroux, and F. Billaud, "Methane pyrolysis: Thermodynamics," *Chemical Engineering Science*, vol. 52, no. 5, pp. 815–827, 1997.

[70] M. Wullenkord, "Determination of Kinetic Parameters of the Thermal Dissociation of Methane," Ph.D. dissertation, Lehrstuhl für Solartechnik (DLR), 2012.

[71] M. Losurdo, M. M. Giangregorio, P. Capezzuto, and G. Bruno, "Graphene CVD growth on copper and nickel: role of hydrogen in kinetics and structure," *Physical Chemistry Chemical Physics*, vol. 13, no. 46, p. 20836, 2011.

[72] I. Alstrup, I. Chorkendorff, and S. Ullmann, "The interaction of ch4 at high temperatures with clean and oxygen precovered cu (100)," *Surface Science*, vol. 264, no. 1-2, pp. 95–102, 1992.

[73] B. Luo, E. Gao, D. Geng, H. Wang, Z. Xu, and G. Yu, "Etching-Controlled Growth of Graphene by Chemical Vapor Deposition," *Chemistry of Materials*, vol. 29, no. 3, pp. 1022–1027, 2017.

[74] S. Chaitoglou and E. Bertran, "Effect of pressure and hydrogen flow in nucleation density and morphology of graphene bidimensional crystals," *Materials Research Express*, vol. 3, no. 7, p. 075603, 2016.

[75] Y. Zhang, Z. Li, P. Kim, L. Zhang, and C. Zhou, "Anisotropic hydrogen etching of chemical vapor deposited graphene," *ACS Nano*, vol. 6, no. 1, pp. 126–132, 2012.

[76] V. Miseikis, D. Convertino, N. Mishra, M. Gemmi, T. Mashoff, S. Heun, N. Haghighian, F. Bisio, M. Canepa, V. Piazza, and C. Coletti, "Rapid CVD growth of millimetre-sized single crystal graphene using a cold-wall reactor," *2D Materials*, vol. 2, no. 1, p. 014006, 2015.

[77] R. Muñoz and C. Gómez-Aleixandre, "Review of CVD synthesis of graphene," *Chemical Vapor Deposition*, vol. 19, no. 10-12, pp. 297–322, 2013.

[78] X. Li, W. Cai, L. Colombo, and R. S. Ruoff, "Evolution of graphene growth on Ni and Cu by carbon isotope labeling," *Nano Letters*, vol. 9, no. 12, pp. 4268–4272, 2009.

[79] J. Lander, H. Kern, and A. Beach, "Solubility and diffusion coefficient of carbon in nickel: Reaction rates of nickel-carbon alloys with barium oxide," *Journal of Applied Physics*, vol. 23, no. 12, pp. 1305–1309, 1952.

[80] W. J. Arnoult and R. B. McLellan, "The solubility of carbon in rhodium ruthenium, iridium and rhenium," *Scripta Metallurgica*, vol. 6, no. 10, pp. 1013–1018, 1972.

[81] S. M. Kim, A. Hsu, Y.-H. Lee, M. Dresselhaus, T. Palacios, K. K. Kim, and J. Kong, "The effect of copper pre-cleaning on graphene synthesis," *Nanotechnology*, vol. 24, no. 36, p. 365602, 2013.

[82] I. Ruiz, W. Wang, A. George, C. S. Ozkan, and M. Ozkan, "Silicon Oxide Contamination of Graphene Sheets Synthesized on Copper Substrates via Chemical Vapor Deposition," *Advanced Science, Engineering and Medicine*, vol. 6, no. 10, pp. 1070–1075, 2014.

[83] G. H. Han, F. Güneş, J. J. Bae, E. S. Kim, S. J. Chae, H. J. Shin, J. Y. Choi, D. Pribat, and Y. H. Lee, "Influence of copper morphology in forming nucleation seeds for graphene growth," *Nano Letters*, vol. 11, no. 10, pp. 4144–4148, 2011.

[84] A. Castellanos-Gomez, M. Buscema, R. Molenaar, V. Singh, L. Janssen, H. S. J. van der Zant, and G. A. Steele, "Deterministic transfer of two-dimensional materials by all-dry viscoelastic stamping," *2D Materials*, vol. 1, no. 1, p. 011002, 2014.

[85] X. Liang, B. a. Sperling, I. Calizo, G. Cheng, C. A. Hacker, Q. Zhang, Y. Obeng, K. Yan, H. Peng, Q. Li, X. Zhu, H. Yuan, A. R. Hight Walker, Z. Liu, L. M. Peng, and C. A. Richter, "Toward clean and crackless transfer of graphene," *ACS Nano*, vol. 5, no. 11, pp. 9144–9153, 2011.

[86] L. G. Cançado, A. Jorio, E. H. M. Ferreira, F. Stavale, C. A. Achete, R. B. Capaz, M. V. O. Moutinho, A. Lombardo, T. S. Kulmala, and A. C. Ferrari, "Quantifying defects in graphene via Raman spectroscopy at different excitation energies," *Nano Letters*, vol. 11, no. 8, pp. 3190–3196, 2011.

[87] L. S. Taylor and G. Zografi, The quantitative analysis of crystallinity using FT-Raman spectroscopy, vol. 15, no. 5, pp. 755–761, 1998.

[88] J. Yan, Y. Zhang, P. Kim, and A. Pinczuk, "Electric field effect tuning of electron-phonon coupling in graphene," *Physical Review Letters*, vol. 98, no. 16, pp. 1–4, 2007.

[89] A. C. Ferrari and D. M. Basko, "Raman spectroscopy as a versatile tool for studying the properties of graphene." *Nature Nanotechnology*, vol. 8, no. 4, pp. 235–46, apr 2013.

[90] C. Thomsen and S. Reich, "Double Resonant Raman Scattering in Graphite," *Physical Review Letters*, vol. 85, no. 24, pp. 5214–5217, 2000.

[91] D. M. Basko, S. Piscanec, and A. C. Ferrari, "Electron-electron interactions and doping dependence of the two-phonon Raman intensity in graphene," *Physical Review B*, vol. 80, no. 16, p. 165413, 2009.

[92] F. Adar, E. Lee, S. Mamedov, and A. Whitley, "Raman Imaging : Defining the Spatial Resolution of the Technology Chemical images of polystyrene beads on silicon acquired using Raman mapping and image," *Spectroscopy Supplement: Raman*, vol. 1-3, no. June, pp. 38–43, 2006.

[93] S. Nagarajan and M. Sopanen, "Non-destructive method for strain imaging in an individual GaN nanorod by confocal Raman technique," *Journal of Physics D: Applied Physics*, vol. 49, no. 46, p. 465303, 2016.

[94] A. Berkdemir, H. R. Gutiérrez, A. R. Botello-Méndez, N. Perea-López, A. L. Elías, C.-I. Chia, B. Wang, V. H. Crespi, F. López-Urías, J.-C. Charlier,

H. Terrones, and M. Terrones, "Identification of individual and few layers of WS2 using Raman spectroscopy." *Scientific Reports*, vol. 3, p. 1755, 2013.

[95] R. V. Gorbachev, I. Riaz, R. R. Nair, R. Jalil, L. Britnell, B. D. Belle, E. W. Hill, K. S. Novoselov, K. Watanabe, T. Taniguchi, A. K. Geim, and P. Blake, "Hunting for monolayer boron nitride: Optical and raman signatures," *Small*, vol. 7, no. 4, pp. 465–468, 2011.

[96] G. Nandamuri, S. Roumimov, and R. Solanki, "Chemical vapor deposition of graphene films," *Nanotechnology*, vol. 21, no. 14, p. 145604, 2010.

[97] B. Zhang, W. H. Lee, R. Piner, I. Kholmanov, Y. Wu, H. Li, H. Ji, and R. S. Ruoff, "Low-temperature chemical vapor deposition growth of graphene from toluene on electropolished copper foils," *ACS Nano*, vol. 6, no. 3, pp. 2471–2476, 2012.